

Magnetic Methods in Robotics

Jake J. Abbott,¹ Eric Diller,² and Andrew J. Petruska³

¹Department of Mechanical Engineering, University of Utah, Salt Lake City, Utah 84112, USA; email: jake.abbott@utah.edu

²Department of Mechanical and Industrial Engineering, University of Toronto, Toronto, Ontario M5S 3G8, Canada; email: ediller@mie.utoronto.ca

³Department of Mechanical Engineering, Colorado School of Mines, Golden, Colorado 80401, USA; email: apetruska@mines.edu

ANNUAL REVIEWS CONNECT

www.annualreviews.org

- Download figures
- Navigate cited references
- Keyword search
- Explore related articles
- Share via email or social media

Annu. Rev. Control Robot. Auton. Syst. 2020.
3:57–90

First published as a Review in Advance on
October 14, 2019

The *Annual Review of Control, Robotics, and
Autonomous Systems* is online at
control.annualreviews.org

<https://doi.org/10.1146/annurev-control-081219-082713>

Copyright © 2020 by Annual Reviews.
All rights reserved

Keywords

magnetic manipulation, magnetic actuation, microrobotics, medical robotics, haptics, aerospace

Abstract

The goal of this article is to provide a thorough introduction to the state of the art in magnetic methods for remote-manipulation and wireless-actuation tasks in robotics. The article synthesizes prior works using a unified notation, enabling straightforward application in robotics. It begins with a discussion of the magnetic fields generated by magnetic materials and electromagnets, how magnetic materials become magnetized in an applied field, and the forces and torques generated on magnetic objects. It then describes systems used to generate and control applied magnetic fields, including both electro-magnetic and permanent-magnet systems. Finally, it surveys work from a variety of robotic application areas in which researchers have utilized magnetic methods, including microrobotics, medical robotics, haptics, and aerospace.

1. INTRODUCTION

Over approximately the past two decades, there has been an ever-increasing interest from the robotics community in the application of magnetic methods for remote manipulation and wireless actuation. The vast majority of the research has focused on the control of microrobots under the guidance of an optical microscope (motivated by the fact that other methods of micromanipulation can be overly disruptive to a given task) and the control of micro- and mesoscale *in vivo* medical robots (motivated by the fact that biological tissues are essentially transparent to magnetic fields that are relatively weak and vary relatively slowly). In such applications, the magnetic object being manipulated or actuated is typically many of its own body lengths away from the system generating the controlled magnetic field. The result is that the magnetic field does not change greatly over the body of the manipulated object, and simply knowing the properties of the magnetic field at the body's center of mass is sufficient to accurately model the resulting force and torque—a simplification that facilitates real-time control. There has been a rapid expansion in the sophistication of magnetic methods in robotics. Many problems are now essentially solved, and a number of conventions and best practices have emerged.

Our goal with this article is to provide a first course in magnetic methods for readers from the robotics community who are interested in applying magnetic methods to their own remote-manipulation and wireless-actuation problems. We assume a knowledge of linear algebra, calculus, and traditional robotics (1) but assume no prior knowledge of magnetics. Our primary motivation is to provide a solid tutorial on the topic rather than an exhaustive review of the literature. Along the way, we reference those who have made key contributions. Throughout the article, we use a consistent notation convention to help the reader quickly discern the types of quantities being represented (see the sidebar titled *Notation*). Our convention sometimes runs counter to the conventions used in prior works.

There is a long tradition of design and control of magnetic devices (2), including motors and other sensors and actuators. In such devices, the system elements are typically in close proximity to one another. For example, consider the permanent-magnet rotor and the electromagnetic stator in a brushless DC motor, which nearly touch one another. In such devices, the magnetic coupling, which typically utilizes Lorentz force, is extremely strong, leading to efficient transfer of power. However, the magnetic interaction is extremely complex, making closed-form analysis challenging in all but the simplest of systems. Concepts such as reluctance and flux linkage have been developed to aid in design, but the understanding of such systems still relies heavily on finite-element analysis (FEA) methods. The modeling assumptions made in those methods are significantly different from those of the manipulation or actuation problems of interest in this article, which typically have components spaced relatively far apart. We do not discuss traditional magnetic devices further, nor do we make use of their specialized design and analysis tools.

2. MAGNETIC FIELDS GENERATED BY MAGNETIC OBJECTS

Magnetic fields originate from the movement of electric charge, which can take the form of an electric current, or electron movement inside a magnetized material. Magnetic fields are vector fields, meaning they are vector-valued functions of position, $\mathbf{b}(\mathbf{P}_b)$, where \mathbf{P}_b is a position (units m, when expressed in some coordinate reference frame) and \mathbf{b} is the magnetic-field vector (units T) there. We are particularly interested in magnetic fields that are projected into space by some source in order to generate forces and torques on magnetic objects for the purpose of manipulation or actuation.

Maxwell's equations form the foundation of classical electromagnetism (3). They explain how the magnetic field \mathbf{b} and the electric field \mathbf{e} are coupled in time and space in a given medium,

NOTATION

Scalars are represented by lowercase standard symbols (e.g., s) and matrices by uppercase blackboard-bold symbols (e.g., \mathbb{M}). We use bold lowercase for vectors (e.g., $\mathbf{v} = [v_x \ v_y \ v_z]^\top$) and bold uppercase for positions (e.g., $\mathbf{P} = [p_x \ p_y \ p_z]^\top$). A left superscript indicates a quantity being represented with respect to a certain frame (e.g., ${}^i\mathbf{v}$ indicates the vector \mathbf{v} expressed in frame i); in equations in which no frame designation is provided, the equation is invariant to the particular frame, provided that each quantity in the equation is expressed with respect to the same frame. The sum of two vectors is a vector, the sum of a position and a vector is a position, the subtraction of two positions is a vector, and the sum of two positions is undefined; these operations must occur between quantities expressed with respect to the same frame.

Uppercase standard symbols (e.g., C) represent $n \times 1$ column arrays that comprise any combination of scalars and vectors. $C(i)$ is the i th element of such an array. The 2-norm of any such array, which includes vectors, is represented by $\|C\|$; such a norm is meaningful only if the elements have consistent units.

The hat notation indicates a vector that is unit length (e.g., $\hat{\mathbf{v}} = \mathbf{v}/\|\mathbf{v}\|$).

${}^j\mathbb{R}_i$ represents a rotation matrix that describes the orientation of frame i with respect to frame j and also maps vectors expressed in frame i into the respective vectors expressed in frame j (e.g., ${}^j\mathbf{v} = {}^j\mathbb{R}_i {}^i\mathbf{v}$). ${}^j\mathbb{T}_i$ represents a homogeneous transformation matrix that describes the pose (i.e., position and orientation) of frame i with respect to frame j and also maps vectors and positions expressed in frame i into the respective vectors and positions expressed in frame j (e.g., ${}^j\mathbf{v} = {}^j\mathbb{T}_i {}^i\mathbf{v}$, ${}^j\mathbf{P} = {}^j\mathbb{T}_i {}^i\mathbf{P}$), assuming that homogeneous coordinates are used (i.e., $\mathbf{v} = [v_x \ v_y \ v_z \ 0]^\top$, $\mathbf{P} = [p_x \ p_y \ p_z \ 1]^\top$).

The function $\mathbb{S}\{\mathbf{v}\}$ indicates the skew-symmetric matrix packing of a vector used in the cross-product operation (e.g., $\mathbf{a} \times \mathbf{b} = \mathbb{S}\{\mathbf{a}\}\mathbf{b}$), which takes the form

$$\mathbb{S}\{\mathbf{v}\} = \begin{bmatrix} 0 & -v_z & v_y \\ v_z & 0 & -v_x \\ -v_y & v_x & 0 \end{bmatrix}.$$

The gradient operator represents partial derivatives in each of the three basis directions of a given frame, which takes the form $\nabla = [\frac{\partial}{\partial x} \ \frac{\partial}{\partial y} \ \frac{\partial}{\partial z}]^\top$.

\mathbb{I}_n is an $n \times n$ identity matrix, and $0_{n \times m}$ is an $n \times m$ block of zeros.

and they ultimately constrain the magnetic fields that can be generated by any system. Maxwell's equations in their entirety are too onerous for applications in robotics, which have relatively slow dynamics. The progress that the robotics community has made in this field is due in part to appropriate quasi-static simplifications and selective application of Maxwell's equations. Furthermore, the practical considerations related to safely generating large electric fields mean that electrostatic contributions are typically negligible in robotics applications. Given these simplifications, one of the pertinent equations tells us that, in general,

$$\nabla \cdot \mathbf{b} = 0 \implies \frac{\partial b_x}{\partial x} + \frac{\partial b_y}{\partial y} + \frac{\partial b_z}{\partial z} = 0. \quad 1.$$

Another pertinent equation puts a constraint on the curl of \mathbf{b} at a given point in space based on the electric current flowing through that point and the time derivative in the electric field at that point. For our purposes, we can assume there is no current flow at the given point we are considering, and the field will be curl free:

$$\nabla \times \mathbf{b} = \mathbf{0} \implies \frac{\partial b_z}{\partial y} = \frac{\partial b_y}{\partial z}, \quad \frac{\partial b_x}{\partial z} = \frac{\partial b_z}{\partial x}, \quad \frac{\partial b_y}{\partial x} = \frac{\partial b_x}{\partial y}. \quad 2.$$

2.1. The Magnetic Dipole Field (Approximation) and the Multipole Expansion

As we consider the field generated by a magnet from an increasingly distant vantage point, whether it be an electromagnet or an object made of magnetized material, the object appears to shrink down to a point, and it becomes difficult to see the nuances of the field shape that are due to the specific geometry of the magnet. Rather, it appears that the field is being generated from a single point \mathbf{P}_m by a magnetic dipole \mathbf{m} (units $\text{A}\cdot\text{m}^2$), which has both a strength and a direction, with the field \mathbf{b} at each point \mathbf{P}_b described by

$$\mathbf{b}(\mathbf{P}_b, \mathbf{m}, \mathbf{P}_m) = \left(\frac{\mu_0}{4\pi \|\mathbf{P}_b - \mathbf{P}_m\|^5} (3 (\mathbf{P}_b - \mathbf{P}_m) (\mathbf{P}_b - \mathbf{P}_m)^\top - \|\mathbf{P}_b - \mathbf{P}_m\|^2 \mathbb{I}_3) \right) \mathbf{m}, \quad 3.$$

where $\mu_0 = 4\pi \times 10^{-7} \text{ T}\cdot\text{m}\cdot\text{A}^{-1}$ is the permeability of free space (Figure 1).

The dipole relationship is commonly represented in the literature as

$$\mathbf{b}(\mathbf{r}, \mathbf{m}) = \left(\frac{\mu_0}{4\pi \|\mathbf{r}\|^3} (3 \hat{\mathbf{r}} \hat{\mathbf{r}}^\top - \mathbb{I}_3) \right) \mathbf{m}, \quad 4.$$

where $\mathbf{r} = \mathbf{P}_b - \mathbf{P}_m$. The strength of a dipole field decays cubically with distance. At any given distance from the dipole, the field is twice as strong along the axis of the dipole (i.e., $\mathbf{r} \parallel \mathbf{m}$) as it is along the axes orthogonal to the dipole (i.e., $\mathbf{r} \perp \mathbf{m}$). Finally, there is a “magic angle” of approximately 54.7° between the \mathbf{m} axis and \mathbf{r} at which $\mathbf{b} \perp \mathbf{m}$.

The discussion above considers the field of a magnet viewed from infinitely far away; in practice, we only need to be far enough away that the vectors from a given point of interest to each location on the magnet are negligibly different from one another. But as we consider locations closer to the magnet in which that assumption is not accurate, the magnet cannot reasonably be modeled as existing at a point, and the dipole model loses accuracy. Magnets are typically quite compact in their design—including both permanent-magnet geometries (e.g., cubes and cylinders) and electromagnets (e.g., cylinders)—and they typically have a magnetic strength that is

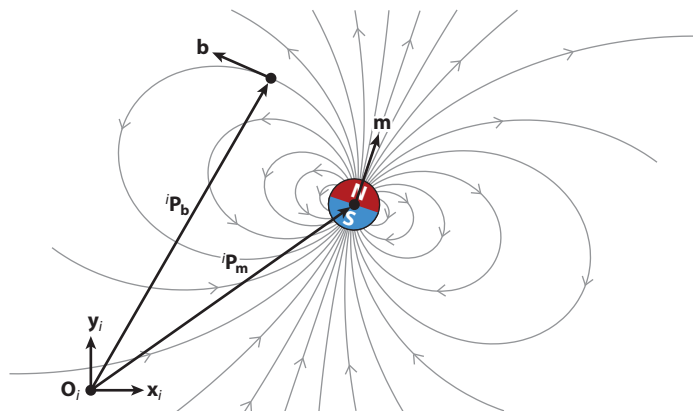


Figure 1

A magnetic dipole, represented by a vector \mathbf{m} at position \mathbf{P}_m , generates a dipole field with streamlines exiting the north pole and entering the south pole. The field is radially symmetric about \mathbf{m} . A magnetic-field vector \mathbf{b} is generated tangent to the streamline at any given point \mathbf{P}_b . All of these vectors and positions can be described with respect to any given coordinate frame i .

distributed fairly uniformly over their volume. As a result, a multipole expansion

$$\mathbf{b}(\mathbf{r}, \mathbf{m}) = \left(\frac{\mu_0}{4\pi \|\mathbf{r}\|^3} \mathbb{T}_1\{\hat{\mathbf{r}}\} + \frac{\mu_0}{4\pi \|\mathbf{r}\|^5} \mathbb{T}_2\{\hat{\mathbf{r}}\} + \frac{\mu_0}{4\pi \|\mathbf{r}\|^7} \mathbb{T}_3\{\hat{\mathbf{r}}\} + \dots \right) \mathbf{m} \quad 5.$$

with even a small number of terms (see Section 7) can be an accurate approximation of the magnetic field \mathbf{b} at location \mathbf{P}_b , measured with respect to the center of mass \mathbf{P}_m . The first term in this expansion is the dipole field of Equation 3, which decays with distance as $\propto \|\mathbf{r}\|^{-3}$; the next term is the quadrupole field, which decays with distance as $\propto \|\mathbf{r}\|^{-5}$; and so forth. Note that the \mathbb{T} matrices are shape functions that are independent of the distance from the source. The terms that follow the dipole-field term describe the deviations in the field from that of the dipole alone, but the contributions of those terms decay away with distance more rapidly than that of the dipole field. As a result, as we consider the field of magnetic sources, we find that approximating the field using only the dipole model of Equation 3 becomes increasingly accurate with increasing distance in general.

2.2. Magnetic Fields from Magnetized Objects

Magnetization is discussed in Section 3. For now, let us simply assume that each differential volume of the material dv (units m^3) has a magnetization $\boldsymbol{\psi}$ (units $A \cdot m^{-1}$), which can be thought of as magnetic density, with a resulting differential magnetic dipole $d\mathbf{m} = \boldsymbol{\psi} dv$ located at point \mathbf{P}_{dm} . The differential magnetic field $d\mathbf{b}$ at some point \mathbf{P}_b due to each differential dipole $d\mathbf{m}$ can be found using Equation 3. To compute the magnetic field $\mathbf{b}(\mathbf{P}_b)$, we then integrate over the volume of the object.

A useful alternate method to calculate the field generated by such a magnet is use of the charge model (2). Essentially, the magnetization of a magnet is replaced by equivalent positive and negative charges on the north- and south-pole faces, respectively, and then the field calculation involves an integration over those surfaces (rather than an integration over the volume), using a methodology developed for electric fields.

The field generated by a uniformly magnetized sphere is perfectly modeled by the dipole model of Equation 3. Any other geometry requires the multipole expansion of Equation 5. However, due to the simple structure of the dipole model, it is common to assume a dipole field for other geometries, with the dipole calculated as the product of an average magnetization and the volume of the object, and assumed to be at the center of mass of the object (although that is not strictly necessary). For common geometries, the modeling error associated with the dipole-field model, as well as the geometric parameters that minimize this error, are described in Reference 4.

The fields of magnetic objects are homothetic, which can be useful in system design. If we consider the field generated by a magnetic object of a given geometry and a given magnetization $\boldsymbol{\psi}$, and we scale only the object's size, we find that the field map shrinks or stretches with the scaled object. For example, if we consider a magnetic sphere of diameter d , the field at a distance d measured normal to the north pole will be the same regardless of the value of d . One consequence of the homothetic property is that large magnets project their fields farther into space than do small magnets (if we consider a field of some given magnitude); this result is quite intuitive. Another consequence is that if we consider a location in the magnetic field with some given magnitude, we find that the spatial derivatives in the field are smaller for larger magnets; this is the case because, with a larger magnet, the field is changing less rapidly in space due to the homothetic property. This actually leads to smaller forces (see Section 4) being generated on a magnetic object placed in the field at a given strength for the larger magnet, which can be counterintuitive.

2.3. Magnetic Fields from Electric Currents

To compute the magnetic field \mathbf{b} generated at any position \mathbf{P}_b due to an electric current i (units A) flowing through a conductor (e.g., a coil of wire), we use the Biot–Savart law to compute the differential field component $d\mathbf{b}$ due to the current flowing through a differential length $d\mathbf{l}$ (units m) of the conductor at one specific location \mathbf{P}_{dl} . If we integrate the effect of each point along the length of the conductor, we arrive at the magnetic field at \mathbf{P}_b :

$$\mathbf{b}(\mathbf{P}_b, i) = \int d\mathbf{b} = \int \mu_0 \frac{i d\mathbf{l} \times (\mathbf{P}_b - \mathbf{P}_{dl})}{4\pi \|\mathbf{P}_b - \mathbf{P}_{dl}\|^3} = \frac{\mu_0 i}{4\pi} \int \frac{\mathbb{S}\{\mathbf{P}_{dl} - \mathbf{P}_b\}}{\|\mathbf{P}_b - \mathbf{P}_{dl}\|^3} d\mathbf{l}. \quad 6.$$

We see that the field at every point in space is linear with respect to current.

When we calculate the field generated by a straight wire, we find a field that circulates around the wire using the right-hand rule: The thumb points in the direction of current flow, and the fingers then curl in the direction of the circulating field. If we form a wire into a small circular loop, the result is a field that looks much like the dipole field of **Figure 1**.

The field of any such object can be described by the multipole expansion of Equation 5 and will have a dipole moment \mathbf{m} , which is calculated as

$$\mathbf{m}(i) = \frac{i}{2} \int \mathbb{S}\{\mathbf{P}_{dl} - \mathbf{P}_{ref}\} d\mathbf{l}, \quad 7.$$

where \mathbf{P}_{ref} is any fixed reference point. Note that the dipole is linear with respect to current. For a circular loop of thin wire with radius r (units m), $\mathbf{m} = \pi r^2 i \hat{\mathbf{a}}$, where $\hat{\mathbf{a}}$ is the winding axis direction, which is governed by the right-hand rule: The fingers are curled in the direction of current flow, and the thumb then points in the direction of $\hat{\mathbf{a}}$. For cylindrical coils with inner radius r_i and thickness t , $\mathbf{m} = \frac{\pi}{3} (3r_i^2 + 3r_i t + t^2) i \hat{\mathbf{a}}$. For noncylindrical coils, the dipole can be approximated as the product of the total circulating current i and the area of the loop.

It is common in the design of electromagnets to make use of a current density j (units $\text{A} \cdot \text{m}^{-2}$). The current flowing through a conductor (e.g., wire) of cross-sectional area a (units m^2) is $i = aj$. Thinking in terms of current density often facilitates the design of electromagnets before explicitly choosing a specific wire gauge, amplifier, and power supply.

The homothetic scaling seen in the fields of magnetized objects is not seen with electromagnets. When scaling the size of an electromagnet (e.g., the radius of the loop r , as well as the cross-sectional area a , by the same ratio), neither maintaining a constant current nor maintaining a constant current density will result in a field that scales homothetically.

3. MAGNETIZATION

In this section, we describe how an object made of magnetic material becomes magnetized when subjected to an applied magnetic field generated by another source. We assume that the object is small relative to the local changes in the applied magnetic field, which is used to ensure that magnetic effects, which are distributed across the volume of the object, can reasonably be approximated as a lumped effect at the center of mass of the object. The result of this assumption is that for a body of volume v , the magnetic dipole of the body is related to the average magnetization ψ as $\mathbf{m} = v\psi$. When considering magnetization, it is customary to represent the applied magnetic field as $\mathbf{h} = \mathbf{b}/\mu_0$ (units $\text{A} \cdot \text{m}^{-1}$), which is sometimes referred to as the auxiliary magnetic field (3). We are ultimately interested in calculating the magnetic dipole of the object as a function of the applied field, $\mathbf{m}(\mathbf{h})$, which will enable us to compute forces and torques on the magnetized object due to the applied field (see Section 4). In general, the relationship between the applied field

and the magnetization of an object is given by the (dimensionless) apparent susceptibility tensor ${}^o\mathbb{X}_a\{\mathbf{h}\}$ (most easily defined in the object frame), which is a function of the geometry of the object, the bulk material property, and the field it is subjected to, leading to

$${}^o\mathbf{m}\{\mathbf{h}\} = v {}^o\mathbb{X}_a\{\mathbf{h}\} {}^o\mathbf{h}. \quad 8.$$

For complex geometries, this relationship is best calculated using FEA methods, whereas analytical models exist for simple geometries.

The nature of the apparent susceptibility tensor is a function of the size of the object. Below, we consider macro- and mesoscale objects separately from micro- and nanoscale objects. The nature of the apparent susceptibility tensor is also a function of the type of magnetic material. We focus on ferromagnetic and superparamagnetic materials, which have proven to be practically useful in the context of robotic manipulation or actuation, due to their relatively strong response to an applied field. Readers interested in other forms of magnetization (e.g., diamagnetism) are referred to References 2 and 5.

3.1. Magnetization of Macro- and Mesoscale Objects

Most engineered magnets used in robotics are large enough that we can assume a polycrystalline object with many randomly oriented grains, such that shape anisotropy (i.e., the effect of geometry) dominates over crystalline anisotropy in determining magnetization. There is a lower size limit on the validity of such an assumption; micro- and nanoscale objects are discussed in Section 3.2.

When we discuss “magnetic materials,” we are typically referring to ferromagnetic materials, which are materials whose magnetic properties are strongly influenced by the presence of an applied magnetic field. All materials have the potential to be magnetic, due to the presence of electrons within the material, but in most materials the magnetic contribution of the electrons tends to average to zero when integrated over the volume of the material. In ferromagnetic materials, however, an applied field causes the contributions of the electrons to organize, resulting in a net magnetization that is nonzero. Different materials and objects of different geometries have different history-dependent input–output relationships between the applied field and the resulting magnetization. The results needed to understand how ferromagnetic materials become magnetized in an applied magnetic field are available in a number of textbooks on magnetism and magnetic materials (2, 5). We provide a simplified summary here that will be sufficient for use in robotic applications.

Let us refer to the magnetic field within the magnetic material as \mathbf{h}_{in} . At any given location in the material, the magnetization is related to the internal field by the (dimensionless) susceptibility of the material, $\chi\{\mathbf{h}_{\text{in}}\}$, which is a bulk material property, as $\boldsymbol{\psi} = \chi\{\mathbf{h}_{\text{in}}\}\mathbf{h}_{\text{in}}$. In general, the susceptibility is itself a history-dependent function of \mathbf{h}_{in} and cannot be assumed to be constant. The material’s permeability μ (units $\text{T}\cdot\text{m}\cdot\text{A}^{-1} = \text{N}\cdot\text{A}^{-2}$) and its susceptibility are related by $\mu = \mu_0(1 + \chi)$, so μ is also history dependent in general.

The magnetization curve of a general ferromagnetic material is depicted in **Figure 2a**. A few features are worth noting. First, there is hysteresis (i.e., the magnetization is a function of both the current and previous values of the field). Second, there is an asymptotic approach to a saturation ψ_{sat} . Third, there is a characteristic slope of the curve near $\|\boldsymbol{\psi}\| = 0$, which is considered the nominal susceptibility of the material. Fourth, when the field returns to zero, in general the magnetization does not also return to zero; if the material has previously been brought to saturation, then bringing the field to zero will cause the magnetization to be equal to the remanent magnetization ψ_r , and it takes a coercive field \mathbf{h}_c to bring the magnetization

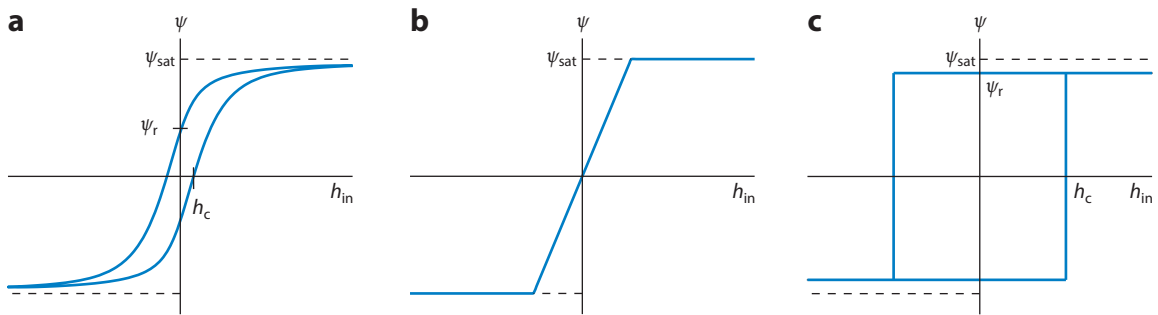


Figure 2

Magnetization of (a) general ferromagnetic materials, (b) ideal soft-magnetic materials as well as paramagnetic materials, and (c) ideal permanent-magnet materials. In this common representation, the internal field and the magnetization are represented by their scalar projections (i.e., signed magnitudes) in any given direction within the material and are independent of object geometry.

back to zero. Materials with low coercivity are known as soft-magnetic materials, and those with high coercivity are known as hard-magnetic materials. A review of macroscopic models of magnetization that include hysteresis can be found in Reference 6. However, much of the work applying magnetic methods in robotics has avoided traversing the hysteresis loop of hysteretic materials during use because of the complexity of the response [with a few exceptions (7)]. Instead, most robotics work uses materials that can be assumed to be either perfectly soft or perfectly hard.

At the extreme of soft-magnetic materials we find materials in which the hysteresis is negligible, and we can use the ideal model depicted in **Figure 2b**. In the context of robotics, these materials can be modeled as having linear magnetization up to the point of saturation, with no history dependence. In the magnetization of real materials, the sharp corner in the model will actually exhibit a smooth transition between the linear asymptote and the saturation asymptote; this adds only a small amount of error in the model, over a relatively small range of field values. Ideal soft-magnetic materials are the typical choice for the cores of electromagnets. They can also be used in devices designed to be manipulated or actuated.

At the extreme of hard-magnetic materials we find materials in which the magnetization is insensitive to the field over a large range; these are permanent-magnet materials. In the context of robotics, we can use the ideal model depicted in **Figure 2c**. The magnetization is assumed to be constant at the remanent magnetization (which is typically somewhat less than the saturation magnetization). In the magnetization of real materials, the constant-magnetization regions of the model will not be perfectly constant; however, this assumption adds only a small amount of error in the model unless the field is very strong (typically well beyond the strength of fields generated in remote-manipulation and wireless-actuation applications).

Although ψ and \mathbf{h}_{in} are always parallel, \mathbf{h} and \mathbf{h}_{in} (and thus \mathbf{h} and ψ) are not necessarily parallel. The origins of the apparent susceptibility tensor in Equation 8 are as follows. In any given direction x (without loss of generality), the magnitude of the internal field is a function of the magnitude of the applied field in that direction and a demagnetizing field proportional to the magnetization in that direction: $h_{in,x} = h_x - n_{dx}\psi_x$. Here, n_{dx} is the geometry-dependent demagnetization factor in the x direction of the object. We find that $n_{dx} \rightarrow 0$ as the geometry in the x direction becomes longer relative to other dimensions of the object, and $n_{dx} \rightarrow 1$ as it becomes relatively shorter. A direction of the object in which n_d is a local minimum is referred to as an easy axis of the object (i.e., easy to magnetize).

3.1.1. Magnetization of soft-magnetic spheres and ellipsoids. A sphere is the simplest of all geometries, described by a single parameter, which leads to simple magnetization characteristics. The demagnetization factor is $n_d = 1/3$ in every direction, and $\boldsymbol{\psi} \parallel \mathbf{h}$. In terms of the magnitude of $\boldsymbol{\psi}$, there is a linear-magnetization region and a saturated region:

$$\|\boldsymbol{\psi}\| = \begin{cases} 3\|\mathbf{h}\|, & \|\mathbf{h}\| \leq \psi_{\text{sat}}/3, \\ \psi_{\text{sat}}, & \|\mathbf{h}\| \geq \psi_{\text{sat}}/3. \end{cases} \quad 9.$$

Ellipsoids are the second-simplest geometry to consider, due to their smoothly varying shape in all three dimensions. The magnetization in the linear-magnetization region can be described by a linear relationship between the applied field vector and the resulting magnetization vector in the object's frame:

$${}^o\boldsymbol{\psi} = {}^o\mathbb{X}_d {}^o\mathbf{h} = \begin{bmatrix} \frac{\chi}{1+\chi n_{dx}} & 0 & 0 \\ 0 & \frac{\chi}{1+\chi n_{dy}} & 0 \\ 0 & 0 & \frac{\chi}{1+\chi n_{dz}} \end{bmatrix} {}^o\mathbf{h} \approx \begin{bmatrix} \frac{1}{n_{dx}} & 0 & 0 \\ 0 & \frac{1}{n_{dy}} & 0 \\ 0 & 0 & \frac{1}{n_{dz}} \end{bmatrix} {}^o\mathbf{h}. \quad 10.$$

The final, approximate equality assumes an object made of material with a high nominal susceptibility being magnetized in relatively weak fields such that $\chi \gg 1$ (which is typical of many remote-manipulation and wireless-actuation tasks), such that the magnetization is dominated by the geometry of the object and is insensitive to the nominal material susceptibility. When using Equation 10, if the magnetization is calculated beyond saturation (i.e., $\|\boldsymbol{\psi}\| > \psi_{\text{sat}}$), then $\|\boldsymbol{\psi}\| = \psi_{\text{sat}}$, and the orientation of $\boldsymbol{\psi}$ can be calculated as described in Reference 8.

Equations to solve for the demagnetization factors for ellipsoids of arbitrary geometry in a uniform magnetic field are known (9, 10); these values are typically accurate approximations in nonuniform fields. Special cases of ellipsoids include prolate ellipsoids, which have an axis of symmetry that is the unique longest dimension of the object, and oblate ellipsoids, which have an axis of symmetry that is the unique shortest dimension of the object. Equations to solve for the demagnetization factors for these symmetrical ellipsoids are provided in Reference 8. Prolate ellipsoids are special ellipsoids in that they have a unique easy axis of magnetization.

3.1.2. Magnetization of nonellipsoidal geometries. Demagnetization factors have been computed for the principal axes of nonellipsoidal objects (11), including cylinders (12, 13), cylindrical shells and rings (14), rectangular prisms (15), and many others. A common approach is to determine the equivalent ellipsoid of the object (13), in order to make use of Equation 10. The calculations of equivalent ellipsoids rely on the assumption of uniform magnetization, implying a very strong applied field, which is not typically the case for robotic manipulation or actuation tasks. Although this method will enable determination of the magnetization along the three principal axes of the object, in general the easy axes of the object may not correspond to any of these principal axes and can in fact vary with the strength of the applied field for shapes that are not highly symmetric. The equivalent ellipsoid method correctly predicts that a cube (which would have a sphere as its equivalent ellipsoid) is isotropic. However, as a counterexample, consider a thin square plate. The equivalent ellipsoid suggests that the shape should have a single hard axis perpendicular to the plate face and be isotropic in the plane of the plate. However, depending on the strength of the applied field, the plate will show an in-plane easy axis along the diagonal or even the edge of the plate (16). Therefore, the ellipsoid approximation sometimes misses these higher-order magnetic responses. Much of the magnetic physics literature on demagnetization factors does not treat these higher-order effects because those studies are often concerned only

with the response along the principal axes. Note also that the three demagnetization factors may not necessarily sum to one for nonellipsoidal bodies like they do for ellipsoids (5). For general nonellipsoidal shapes in robotics, we suggest using experimental or FEA methods to determine the required response directly.

3.2. Magnetization of Micro- and Nanoparticles

At very small sizes (typically below 1 μm), magnetic materials tend to exhibit a different behavior than they do at larger sizes. This change is due to the particles being on the scale of individual magnetic domains and thus losing their characteristic ferromagnetic response, which depends on magnetic interactions between domains.

Some materials used for micro- or nanorobotics that are ferromagnetic at large sizes exhibit a special class of magnetic response known as superparamagnetism when at submicrometer size (17). This response is a class of paramagnetism whereby magnetic moments in the material can be aligned with an applied magnetic field in opposition to the randomizing effect of thermal fluctuations. Many materials exhibit paramagnetism at any size; superparamagnetism is the term used for those that are ferromagnetic at larger sizes and have a much larger susceptibility. Superparamagnetic nanoparticles thus exhibit a strong soft-magnetic response, which has enabled their use in microrobotic manipulation for targeted drug delivery in the human body, most often using superparamagnetic iron-oxide nanoparticles (18–20). Notably, due to the loss of ferromagnetic response, micro- and nanoparticles typically do not exhibit magnetic coercivity and thus behave like ideal soft-magnetic materials (see **Figure 2b**). Magnetic manipulation of micro- and nanoparticles is thus similar to that of larger soft magnets.

Under certain conditions, other complex micro- and nanoparticle magnetic responses can be seen. For example, very small magnets (smaller than 1 μm , although the size is subject to many factors) will contain only a single magnetic domain. These particles tend to exhibit a moderate magnetic coercivity and high remanence, behaving like a hard magnet.

Micro- and nanoparticles can show anisotropy in magnetization, where nonspherical particles exhibit preferential easy axes of magnetization in the same way as large soft magnets do. This effect is maximized if the physical aspect ratio of the particle is large, as with thin films (21). Even particles that are nearly spherical tend to exhibit a small amount of anisotropy from crystalline or other effects, which enables them to be oriented in a magnetic field.

4. FORCE AND TORQUE ON MAGNETIC OBJECTS

In this section, we show how magnetic objects experience force and torque when subjected to an applied magnetic field generated by another source.

4.1. Force and Torque on a Magnetic Dipole

When a permanent-magnet or electromagnet dipole \mathbf{m} is placed in an applied magnetic field \mathbf{b} , the magnetic dipole is compelled to translate and rotate in an attempt to minimize the magnetic potential energy $-\mathbf{b} \cdot \mathbf{m}$ (i.e., to increase $\mathbf{b} \cdot \mathbf{m}$). In the case of a soft-magnetic dipole \mathbf{m} that is created by an applied field $\mathbf{h} = \mathbf{b}/\mu_0$, the same magnetic potential energy can be used, but with $\|\mathbf{m}\|$ modeled as constant at its instantaneous value.

Let us first consider force. If a translation of \mathbf{m} in a given direction would result in an increase in $\mathbf{b} \cdot \mathbf{m}$, then a magnetic force will be generated in that direction. Since we are considering pure translations of the dipole during the force calculation, \mathbf{m} can be considered constant (in both magnitude and direction) during the spatial differentiation of $\mathbf{b} \cdot \mathbf{m}$. Using the principle of virtual

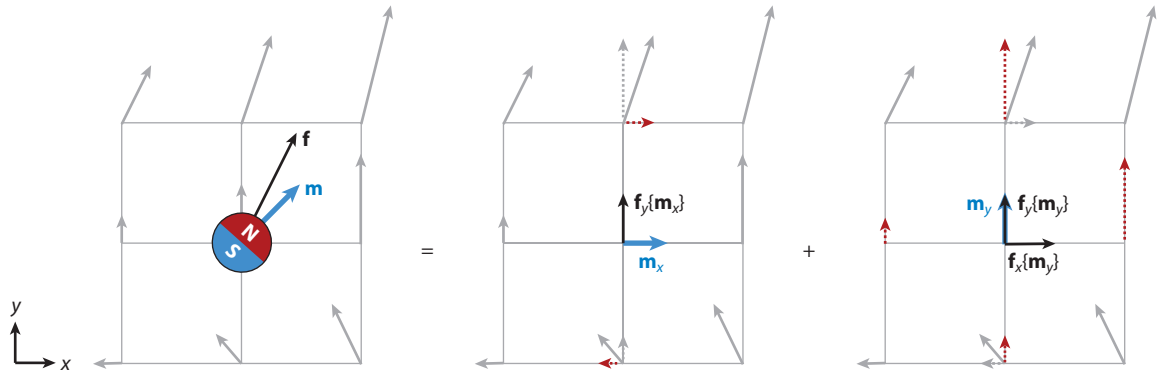


Figure 3

Visualization of force and torque generation. A magnetic force $\mathbf{f} = [1 \ 2 \ 0]^\top$ is generated on a magnetic dipole $\mathbf{m} = [1 \ 1 \ 0]^\top$ in an applied field $\mathbf{b} = [0 \ 2 \ 0]^\top$ with spatial derivatives $\partial b_x/\partial x = 0$, $\partial b_y/\partial y = 1$, $\partial b_z/\partial z = -1$ (not shown), $\partial b_x/\partial y = \partial b_y/\partial x = 1$, $\partial b_x/\partial z = \partial b_z/\partial x = 0$, and $\partial b_y/\partial z = \partial b_z/\partial y = 0$. The magnetic dipole is broken into its components, and the red arrows indicate the field-vector components that contribute to the respective force components. In addition, a magnetic torque (not shown) attempts to align \mathbf{m} (i.e., the component \mathbf{m}_x) with the local field vector \mathbf{b} , resulting in a torque $\boldsymbol{\tau} = [0 \ 0 \ 2]^\top$.

work, without loss of generality, the force (units N) in the x direction is

$$f_x = \frac{\partial(\mathbf{b} \cdot \mathbf{m})}{\partial x} = \frac{\partial(\mathbf{b}^\top \mathbf{m})}{\partial x} = \frac{\partial \mathbf{b}^\top}{\partial x} \mathbf{m}. \quad 11.$$

Combining the results for the individual components, we can express the force vector \mathbf{f} using a function that is linear with respect to \mathbf{m} (see **Figure 3**):

$$\mathbf{f} = \nabla(\mathbf{b} \cdot \mathbf{m}) = \begin{bmatrix} \frac{\partial \mathbf{b}^\top}{\partial x} \mathbf{m} \\ \frac{\partial \mathbf{b}^\top}{\partial y} \mathbf{m} \\ \frac{\partial \mathbf{b}^\top}{\partial z} \mathbf{m} \end{bmatrix} = \begin{bmatrix} \frac{\partial \mathbf{b}}{\partial x} & \frac{\partial \mathbf{b}}{\partial y} & \frac{\partial \mathbf{b}}{\partial z} \end{bmatrix}^\top \mathbf{m} = \begin{bmatrix} m_x \frac{\partial b_x}{\partial x} + m_y \frac{\partial b_y}{\partial x} + m_z \frac{\partial b_z}{\partial x} \\ m_x \frac{\partial b_x}{\partial y} + m_y \frac{\partial b_y}{\partial y} + m_z \frac{\partial b_z}{\partial y} \\ m_x \frac{\partial b_x}{\partial z} + m_y \frac{\partial b_y}{\partial z} + m_z \frac{\partial b_z}{\partial z} \end{bmatrix}. \quad 12.$$

We will refer to $\mathbb{B}_\nabla \equiv \begin{bmatrix} \frac{\partial \mathbf{b}}{\partial x} & \frac{\partial \mathbf{b}}{\partial y} & \frac{\partial \mathbf{b}}{\partial z} \end{bmatrix}$ as the field-derivative matrix, which is symmetric (due to Equation 2) with a trace of zero (due to Equation 1). The force can also be expressed using the compact operator notation on the field \mathbf{b} :

$$\mathbf{f} = (\mathbf{m} \cdot \nabla) \mathbf{b} = \left(m_x \frac{\partial}{\partial x} + m_y \frac{\partial}{\partial y} + m_z \frac{\partial}{\partial z} \right) \mathbf{b} = \begin{bmatrix} m_x \frac{\partial b_x}{\partial x} + m_y \frac{\partial b_y}{\partial x} + m_z \frac{\partial b_z}{\partial x} \\ m_x \frac{\partial b_x}{\partial y} + m_y \frac{\partial b_y}{\partial y} + m_z \frac{\partial b_z}{\partial y} \\ m_x \frac{\partial b_x}{\partial z} + m_y \frac{\partial b_y}{\partial z} + m_z \frac{\partial b_z}{\partial z} \end{bmatrix}. \quad 13.$$

Although not immediately evident, the final equalities in Equations 12 and 13 are equal due to the constraint imposed by Equation 2.

In the formulations above, either the role of the dipole being manipulated or actuated and the spatial derivative of the field are intermingled in the force calculation, or the role of the dipole is factored out linearly. However, it is the spatial derivative of the field that we would typically consider to be the system input that we will control in our generation of force, so it would be preferable to linearly factor out the spatial derivative. In addition, the properties of the field-derivative matrix limit the number of truly independent quantities in any magnetic field. These issues were observed in Reference 22, leading to the following (nonunique) formulation that separates the role of the manipulated dipole from five independent spatial derivatives (i.e., gradients) treated as an input to

the force calculation:

$$\mathbf{f} = \begin{bmatrix} m_x & m_y & m_z & 0 & 0 \\ 0 & m_x & 0 & m_y & m_z \\ -m_z & 0 & m_x & -m_z & m_y \end{bmatrix} \begin{bmatrix} \frac{\partial b_x}{\partial x} & \frac{\partial b_x}{\partial y} & \frac{\partial b_x}{\partial z} & \frac{\partial b_y}{\partial y} & \frac{\partial b_y}{\partial z} \end{bmatrix}^\top \iff \mathbf{f} = \mathbb{M}_G\{\mathbf{m}\}G. \quad 14.$$

The elements of G are drawn from the elements of the field-derivative matrix \mathbb{B}_∇ .

Next, let us consider torque. If a rotation of \mathbf{m} about a given axis would result in an increase in $\mathbf{b} \cdot \mathbf{m}$, then a magnetic torque will be generated about that axis. Without loss of generality, let us consider \mathbf{m} rotated from \mathbf{b} by some angle θ_x (units rad) about the x axis. The restoring torque (units N·m) about the x axis is

$$\tau_x = \frac{\partial(\mathbf{b} \cdot \mathbf{m})}{\partial \theta_x} = \frac{\partial(\|\mathbf{b}\| \|\mathbf{m}\| \cos(\theta_x))}{\partial \theta_x} = -\|\mathbf{b}\| \|\mathbf{m}\| \sin(\theta_x). \quad 15.$$

Combining the results for the individual components, we can express the torque vector $\boldsymbol{\tau}$ as the cross-product between the dipole and the field, with the torque attempting to align the dipole with the field:

$$\boldsymbol{\tau} = \mathbf{m} \times \mathbf{b} = \mathbb{S}\{\mathbf{m}\}\mathbf{b}. \quad 16.$$

An important result of this equation is that $\boldsymbol{\tau}$ is always orthogonal to both \mathbf{m} and \mathbf{b} , so for this single dipole, it is impossible to generate torque about the \mathbf{m} axis, regardless of the magnetic field. This constrains torque generation on a dipole to two degrees of freedom (DOFs), and thus force-torque generation to five DOFs. Another important result is that the maximum torque that can be generated on a permanent-magnet \mathbf{m} in a field with a given strength is achieved when the field is applied orthogonal to the dipole.

4.2. Force and Torque Between Magnetic Dipoles

In Section 4.1, we discussed the force and torque on a magnetic dipole in an arbitrary magnetic field. If the source of the magnetic field can itself be accurately modeled by the magnetic dipole field (Equation 3) at the location of the dipole being manipulated or actuated, then we can be more specific about the applied force and torque.

The field-derivative matrix at location \mathbf{P}_j , generated by a dipole \mathbf{m}_i located at \mathbf{P}_i , is

$$\mathbb{B}_\nabla\{\mathbf{P}_j, \mathbf{m}_i, \mathbf{P}_i\} = \frac{3\mu_0}{4\pi \|\mathbf{r}_{ij}\|^4} \left(\mathbf{m}_i \hat{\mathbf{r}}_{ij}^\top + \hat{\mathbf{r}}_{ij} \mathbf{m}_i^\top + \left(\hat{\mathbf{r}}_{ij}^\top \mathbf{m}_i \right) \left(\mathbb{I}_3 - 5\hat{\mathbf{r}}_{ij} \hat{\mathbf{r}}_{ij}^\top \right) \right), \quad 17.$$

where $\mathbf{r}_{ij} = \mathbf{P}_j - \mathbf{P}_i$, which can be repacked to create the field-derivative array function $G\{\mathbf{P}_j, \mathbf{m}_i, \mathbf{P}_i\}$ for use with Equation 14. Explicitly, then, the force on the dipole \mathbf{m}_j at location \mathbf{P}_j from the field derivative $\mathbb{B}_\nabla\{\mathbf{P}_j, \mathbf{m}_i, \mathbf{P}_i\}$ is

$$\mathbf{f} = \frac{3\mu_0}{4\pi \|\mathbf{r}_{ij}\|^4} \left(\left(\hat{\mathbf{r}}_{ij}^\top \mathbf{m}_j \right) \mathbf{m}_i + \left(\hat{\mathbf{r}}_{ij} \mathbf{m}_i^\top \right) \mathbf{m}_j + \left(\mathbf{m}_i^\top \mathbf{m}_j - 5 \left(\hat{\mathbf{r}}_{ij}^\top \mathbf{m}_i \right) \left(\hat{\mathbf{r}}_{ij}^\top \mathbf{m}_j \right) \right) \hat{\mathbf{r}}_{ij} \right). \quad 18.$$

We see that the magnitude of the field-derivative matrix, and the resulting forces, decay with distance to the fourth power, which is more rapid than the field (and torque, as shown below) decays. It is easy to show that $\mathbb{B}_\nabla\{\mathbf{P}_j, \mathbf{m}_i, \mathbf{P}_i\}\mathbf{m}_j = -\mathbb{B}_\nabla\{\mathbf{P}_i, \mathbf{m}_j, \mathbf{P}_j\}\mathbf{m}_i$; that is, the forces between dipoles are equal and opposite, as should be expected from Newton's laws.

The field of dipole \mathbf{m}_i also imparts a torque on dipole \mathbf{m}_j :

$$\boldsymbol{\tau}\{\mathbf{m}_j, \mathbf{P}_j, \mathbf{m}_i, \mathbf{P}_i\} = \mathbb{S}\{\mathbf{m}_j\}\mathbf{b}\{\mathbf{P}_j, \mathbf{m}_i, \mathbf{P}_i\} = \mathbb{S}\{\mathbf{m}_j\} \left(\frac{\mu_0}{4\pi \|\mathbf{r}_{ij}\|^3} \left(3\hat{\mathbf{r}}_{ij}\hat{\mathbf{r}}_{ij}^\top - \mathbb{I}_3 \right) \right) \mathbf{m}_i. \quad 19.$$

This is simply the combination of Equations 3 and 16. It can be seen that the torque acting on the dipole being manipulated or actuated (i.e., dipole \mathbf{m}_j) is linear with respect to the dipole acting as the field source (i.e., dipole \mathbf{m}_i). However, unlike forces, magnetic torques are not equal and opposite in general.

4.3. Force and Torque on Soft-Magnetic Objects

Permanent-magnet objects are typically approximated as constant-magnitude dipoles, enabling the use of the methods in Section 4.1 directly. Here we consider magnets that are not well approximated as a constant dipole, such as soft magnets. In the most general manner, the first step to determine the force and torque on any magnetic objects in an applied field \mathbf{b} is to first compute the magnetic dipole \mathbf{m} of the object due to the applied field $\mathbf{h} = \mathbf{b}/\mu_0$, using the methods of Section 3.1 for the macro- or mesoscale or those from Section 3.2 for the micro- or nanoscale. The second step is to then compute the force and torque on \mathbf{m} due to \mathbf{b} using the methods in Section 4.1. For many objects, there is not a unique equilibrium orientation of the object in a static field; rather, the orientation is history dependent.

Because spheres and ellipsoids are the simplest geometries in terms of magnetization modeling (see Section 3.1.1), they are the objects for which we have the deepest understanding of the forces and torques generated by an applied field (8). A soft-magnetic sphere magnetizes parallel to the applied field and experiences no alignment torque. The force on a sphere simplifies to $\mathbf{f} = \|\mathbf{m}\| (\nabla \|\mathbf{b}\|)$, where \mathbf{m} is calculated using Equation 9. For an ellipsoid, with a magnetization tensor from Equation 10, the force and torque up to the point of saturation are

$$\begin{bmatrix} {}^i\boldsymbol{\tau} \\ {}^i\mathbf{f} \end{bmatrix} = \frac{v}{\mu_0} \begin{bmatrix} \mathbb{S}\{{}^i\mathbb{X}_a {}^i\mathbf{b}\} & 0_{3 \times 5} \\ 0_{3 \times 3} & \mathbb{M}_G\{{}^i\mathbb{X}_a {}^i\mathbf{b}\} \end{bmatrix} \begin{bmatrix} {}^i\mathbf{b} \\ {}^i_G \end{bmatrix}, \quad 20.$$

where the magnetization tensor has been rotated to correspond with the frame of the other vectors: ${}^i\mathbb{X}_a = {}^i\mathbb{R}_o {}^o\mathbb{X}_a {}^i\mathbb{R}_o^\top$. The torque varies quadratically with the field, and the force varies bilinearly with the field and field derivative (beyond saturation, see Reference 8). If the ellipsoid has unique demagnetization factors, six-DOF torque and force can be applied (although this remains to be demonstrated).

Although complex soft-magnetic shapes are often avoided in robotics, their nonuniform magnetization enables additional capabilities, such as six-DOF manipulation (23). In this case, force and torque are best calculated using FEA methods to first determine the magnetization response within the magnet body. The force and torque can then be modeled as a continuously distributed case of the multidipole object (see Section 4.4).

4.4. Beyond Point Dipoles

Consider an object, with a center of mass at \mathbf{P}_o , in which n magnetic dipoles \mathbf{m}_i are rigidly embedded at n distinct locations \mathbf{P}_i . We will typically know the magnetic dipoles ${}^o\mathbf{m}_i$ and their locations ${}^o\mathbf{P}_i$ expressed in the object frame and will have a homogeneous transformation ${}^w\mathbb{T}_o$ that describes the pose of the object in the workspace frame. The vector ${}^o\mathbf{P}_i - {}^o\mathbf{P}_o$ expressed in the object frame is constant for each magnet since the magnets are rigidly embedded in the object.

When the object is placed in a magnetic field, each of the dipoles experiences a magnetic force \mathbf{f}_i described by Equations 12–14 and a magnetic torque $\boldsymbol{\tau}_i$ described by Equation 16, based on the field and field derivatives at their respective locations. The total force on the object is simply the sum of the individual forces, while the total torque on the object is the sum of the individual torques plus the torques due to forces applied with moment arms relative to the center of mass:

$$\mathbf{f}_o = \sum_{i=1}^n \mathbf{f}_i, \quad \boldsymbol{\tau}_o = \sum_{i=1}^n (\boldsymbol{\tau}_i + \mathbb{S}(\mathbf{P}_i - \mathbf{P}_o) \mathbf{f}_i). \quad 21.$$

Because an independent five-DOF force-torque can be applied to each of the dipoles in general, it is possible to apply a six-DOF force-torque to the object.

Equation 21 is formulated in terms of a finite number of dipoles. However, as described in Section 2.2 in regard to the magnetic-field sources, all magnetic objects will have distributed magnetization, with each differential $d\mathbf{m}$ at a distinct location \mathbf{P}_{dm} in the applied field. Thus, the true force and torque on any magnetic object is calculated using the continuous (integral) version of Equation 21. Consequently, modeling a magnetic object being manipulated or actuated as a point dipole misses some higher-order effects (analogous to Equation 5), but in practice these higher-order effects are relatively small and are typically negligible.

For small enough geometries, it is possible to model the force and torque using the field and field derivative at a single point (24). Using Equations 14 and 16, one can express the force and torque of n individual dipoles as a function of the field and field derivative at the center of mass:

$$\begin{bmatrix} \boldsymbol{\tau}_o \\ \mathbf{f}_o \end{bmatrix} = \left(\sum_{i=1}^n \begin{bmatrix} \mathbb{S}\{\mathbf{m}_i\} & \mathbb{S}\{\mathbf{P}_i - \mathbf{P}_o\} \mathbb{M}_G\{\mathbf{m}_i\} \\ 0_{3 \times 3} & \mathbb{M}_G\{\mathbf{m}_i\} \end{bmatrix} \right) \begin{bmatrix} \mathbf{b}_o \\ G_o \end{bmatrix}. \quad 22.$$

In Section 5, we show how this actuation equation can be further cast in terms of inputs such as currents running through electromagnetic coils. In Reference 24, a primary (central) permanent-magnet dipole is augmented by attaching an additional pair of permanent-magnet dipoles that are antiparallel with each other and perpendicular to the central dipole (among other configurations considered). The conventional five-DOF actuation is still performed on the central dipole, but this configuration enables spatial derivatives in the field to apply a force couple to the two new dipoles, resulting in a torque about the axis of the central dipole. This circumvents the two-DOF torque (five-DOF force-torque) limitation when actuating a single magnetic dipole, enabling full three-DOF torque (six-DOF force-torque). This multidipole concept was further investigated in Reference 25, in which the three-dipole object was replaced by an equivalent two-dipole object, which enabled the respective magnetic components to be varied by changing the angle between the dipoles while maintaining a constant amount of magnetic material in the object. This study found that there is an optimal angle to maximize the new torque DOF, but with an accompanying 61% reduction in the original five-DOF force-torque. It also found that the new torque DOF scales poorly relative to the other five DOFs when the object is reduced in size.

4.5. Magnetic Stability

Earnshaw's theorem tells us that there can be no stable magnetic equilibrium point in a static magnetic field (2). Typically, a magnetic object placed within a field will experience a force-torque that tends to move the magnetic object away from its current location. It is possible to create points within a field in which there is neither magnetic force nor torque (e.g., the center of a Maxwell coil,

as described in Section 5.2), but a small deviation from such a point will result in a force-torque that tends to drive the magnetic object away from the point. A result is that any system designed to manipulate an untethered levitating magnetic object must use feedback control to stabilize the position of the object.

There are certain uses of magnetic fields for manipulation that may at first seem to violate Earnshaw's theorem, but closer inspection reveals that they do not. So-called magnetic traps are sometimes used to manipulate objects under the guidance of an optical microscope. Those objects seem to be drawn to a stable point, and the point is in fact stable in a constrained 2-D plane (e.g., a horizontal microscope slide). However, in such a stable point there is a magnetic force pulling the object into the constraint surface, and if the constraint were to be removed, the object would not remain at that point. A similar phenomenon occurs when a magnetic object is attached to a compliant device (e.g., a magnetic catheter). When such a device is placed in a static magnetic field, it deforms until it reaches an equilibrium pose in which the magnetic force-torque is perfectly balanced by a mechanical reaction force-torque from the compliant device.

Earnshaw's theorem does not apply to diamagnetic materials, which exhibit an opposite magnetic response compared with ferromagnetic materials (that is, the magnetization forms in the direction opposite to the applied field, with $\chi_a < 0$). Diamagnetic materials can levitate stably (or cause the stable levitation of other objects) and have been used in robotic manipulators that utilize ferromagnets levitating over diamagnetic graphite sheets (26).

5. STATIONARY SYSTEMS FOR MANIPULATION AND ACTUATION

5.1. Electromagnetic Control of Magnetic Fields for Manipulation and Actuation

For an arbitrary arrangement of electromagnets—which may include air cores (i.e., no cores), ideal soft-magnetic cores below saturation, other ideal soft-magnetic elements below saturation, or any combination thereof—the magnetic field is linear with respect to the currents flowing through the electromagnets (22, 27). This linear mapping between the applied currents $I = [i_1 \cdots i_n]^T$ (units A) and the field and field gradient at each point \mathbf{P}_b in the workspace can be represented by

$$\begin{bmatrix} b_x \\ b_y \\ b_z \\ \frac{\partial b_x}{\partial x} \\ \frac{\partial b_x}{\partial y} \\ \frac{\partial b_x}{\partial z} \\ \frac{\partial b_y}{\partial x} \\ \frac{\partial b_y}{\partial y} \\ \frac{\partial b_y}{\partial z} \end{bmatrix} = \begin{bmatrix} b_{1x} & \cdots & b_{nx} \\ b_{1y} & \cdots & b_{ny} \\ b_{1z} & \cdots & b_{nz} \\ \frac{\partial b_{1x}}{\partial x} & \cdots & \frac{\partial b_{nx}}{\partial x} \\ \frac{\partial b_{1x}}{\partial y} & \cdots & \frac{\partial b_{nx}}{\partial y} \\ \frac{\partial b_{1x}}{\partial z} & \cdots & \frac{\partial b_{nx}}{\partial z} \\ \frac{\partial b_{1y}}{\partial x} & \cdots & \frac{\partial b_{ny}}{\partial x} \\ \frac{\partial b_{1y}}{\partial y} & \cdots & \frac{\partial b_{ny}}{\partial y} \\ \frac{\partial b_{1y}}{\partial z} & \cdots & \frac{\partial b_{ny}}{\partial z} \end{bmatrix} \begin{bmatrix} i_1 \\ \vdots \\ i_n \end{bmatrix} \iff F = \begin{bmatrix} \mathbf{b} \\ G \end{bmatrix} = \begin{bmatrix} \mathbb{B} \\ \mathbb{G} \end{bmatrix} I = \mathbb{F}_I I. \quad 23.$$

The k th column of the \mathbb{F}_I matrix represents the field array F at the given \mathbf{P}_b that is created by setting current i_k to 1 A and all other currents to 0 A.

Analysis of the \mathbb{F}_I matrix provides insight into how well any electromagnetic system can control the field and field derivative in the workspace. For example, to achieve full force-torque manipulation, all eight terms in the field array F must be independently controllable (i.e., \mathbb{F}_I must be full rank); thus, at least eight sources are necessary (22). \mathbb{F}_I not only can define what is or is not possible for a system, but also can indicate how feasible a control approach is. Let the \mathbb{F}_I matrix be partitioned into its field and field-gradient components as in Equation 23. Then the singular

values of the matrix $\mathbb{G}\mathbb{N}_{\mathbb{B}}$, where $\mathbb{N}_{\mathbb{B}} \equiv (\mathbb{I}_n - \mathbb{B}^\top(\mathbb{B}\mathbb{B}^\top)^\dagger\mathbb{B})$ is the right null space of \mathbb{B} , describe the system's capability to control the field derivative (units $\text{T}\cdot\text{m}^{-1}\cdot\text{A}^{-1}$) independently from the field (22). Likewise, the singular values of $\mathbb{B}\mathbb{N}_{\mathbb{G}}$ describe the system's capability to control the field (units $\text{T}\cdot\text{A}^{-1}$) independently from the field derivative. Together, these two decompositions enable a unit-consistent analysis of the field-generation system as it would be used in a control application.

If we consider the force and torque acting on a permanent-magnet dipole placed in the field, we find that they are linear with respect to the field array, as described in Equations 14, 16, and 22. We can construct an actuation matrix (for lack of a better term) $\mathbb{A}_Y\{\mathbf{P}_b, \mathbf{m}\}$ to map the array of currents to a given output array Y of interest (22, 27):

$$Y = \mathbb{A}_Y\{\mathbf{P}_b, \mathbf{m}\}I = \mathbb{M}_Y\{\mathbf{m}\}\mathbb{F}_I\{\mathbf{P}_b\}I = \mathbb{M}_Y\{\mathbf{m}\}F\{\mathbf{P}_b, I\}. \quad 24.$$

To form the actuation matrix to manipulate a given permanent-magnetic dipole \mathbf{m} , which has a magnitude and an orientation (its position is already encoded in the \mathbb{F}_I matrix), we utilize relations defined in Equations 14 and 16 to construct a manipulation matrix $\mathbb{M}_Y\{\mathbf{m}\}$ matrix, which will take different forms depending on our desired output Y . Similarly to the way that the ability of the system to generate a field array can be analyzed using \mathbb{F}_I , the ability of a magnetic object to be manipulated can be analyzed using \mathbb{M}_Y . Some common manipulation matrices that have been employed are

$$\mathbb{M}_b\{\mathbf{m}\} = \begin{bmatrix} \mathbb{I}_3 & 0_{3 \times 5} \end{bmatrix}, \quad \mathbb{M}_{\tau, f}\{\mathbf{m}\} = \begin{bmatrix} \mathbb{S}\{\mathbf{m}\} & 0_{3 \times 5} \\ 0_{3 \times 3} & \mathbb{M}_G\{\mathbf{m}\} \end{bmatrix}, \quad \mathbb{M}_{b, f}\{\mathbf{m}\} = \begin{bmatrix} \mathbb{I}_3 & 0_{3 \times 5} \\ 0_{3 \times 3} & \mathbb{M}_G\{\mathbf{m}\} \end{bmatrix}, \quad 25.$$

for field, torque and force, and field and force, respectively, where $\mathbb{M}_G\{\mathbf{m}\}$ is defined in Equation 14. \mathbb{M}_b is useful because some magnetic objects will align with the field in an open-loop fashion; the field is often rotated such that magnetic objects will rotate synchronously. $\mathbb{M}_{\tau, f}$ describes the full torque-force wrench on a magnetic object, which is typically employed in closed-loop control. $\mathbb{M}_{b, f}$ is particularly useful in the manipulation of untethered magnetic objects; force is explicitly controlled (which is often used in closed-loop control of position or velocity), but orientation is controlled open-loop by assuming that the magnetic object will continually align itself with the field. When $\mathbb{M}_{b, f}$ is used for the manipulation of untethered magnetic objects, it is typically assumed that the field is changed slowly enough that the object is always aligned with the field, which leads to the assumption $\mathbf{m} = \|\mathbf{m}\|\hat{\mathbf{b}}$, with $\|\mathbf{m}\|$ constant for permanent-magnet objects and calculated based on the local easy axis for soft-magnetic objects (see Section 3).

Given some desired output Y_{des} , the currents can be found using the pseudoinverse (i.e., generalized inverse) of the actuation matrix \mathbb{A}_Y (27), which returns the value that minimizes $\|I\|$ (which is the minimum-power solution if each of the electromagnets has the same resistance) subject to the constraint that the output error $\|Y - Y_{\text{des}}\|$ is minimized:

$$I = \mathbb{A}_Y^\dagger Y_{\text{des}}. \quad 26.$$

When soft-magnetic objects are manipulated, they are magnetized by the applied field as described in Section 3, so the manipulation matrix will depend on the applied field, in which case a linear solution is not possible for some actuation matrices, and nonlinear methods must be employed. Solutions can be framed as a control or optimization problem, such as locally linearizing the system and controlling the change in the output rather than controlling the output directly. The rate of change (using dot notation) of Equation 24 is

$$\dot{Y} = \mathbb{J}_{YI}\{\mathbf{m}, \mathbf{P}_b, I\}\dot{I} = \left(\mathbb{M}_Y\{\mathbf{m}\} + \left[\frac{\partial \mathbb{M}_Y\{\mathbf{m}\}}{\partial F(1)} F \cdots \frac{\partial \mathbb{M}_Y\{\mathbf{m}\}}{\partial F(8)} F \right] \right) \dot{F}, \quad 27.$$

where \mathbb{J}_Y is the Jacobian that maps changes in currents to changes in outputs, $\frac{\partial \mathbb{M}_Y(\mathbf{m})}{\partial \mathbf{F}}$ describes how the manipulation matrix changes with changes in the applied field array, and $\dot{\mathbf{F}} = \mathbb{F}_I\{\mathbf{P}_b\}\dot{\mathbf{I}}$ (i.e., the matrix \mathbb{F}_I is itself a Jacobian of the linear Equation 23).

5.2. Magnetically Orthogonal Systems Based on Specialized Electromagnets

A variety of magnetic systems, particularly early systems, have utilized special types of electromagnets whose fields have simple models by design. These electromagnets are combined in arrangements that create multi-DOF capabilities, where each electromagnet has a specific task that is decoupled from the others (i.e., each electromagnet is responsible for a single term in the field array \mathbf{F}).

The first and most important of these specialized systems is the Helmholtz coil. If two circular coils of equal radius r are arranged coaxially, with the same current i flowing with the same handedness, then the field in the common center of the coils will be locally uniform and aligned with the axial direction, due to the symmetry in the system. That is, because the spatial derivative in the field is zero in each direction, the field near the common center is very similar to that of the field at the common center. A Helmholtz coil is such an arrangement in which the separation distance between the coils is r (Figure 4a), which is optimally uniform in the sense that the second derivative of the field in the axial direction is also zero. The nominal field magnitude is $\|\mathbf{b}\| = (0.72\mu_0/r)i$. It is also possible to make square Helmholtz coils, although they do not exhibit radial symmetry; for square coils of side length l , the separation distance is $0.54l$ (28), and the resulting field magnitude is $\|\mathbf{b}\| = (1.30\mu_0/l)i$. Alternatives to the Helmholtz-coil spacing have been explored with different definitions of optimal that consider the field throughout the

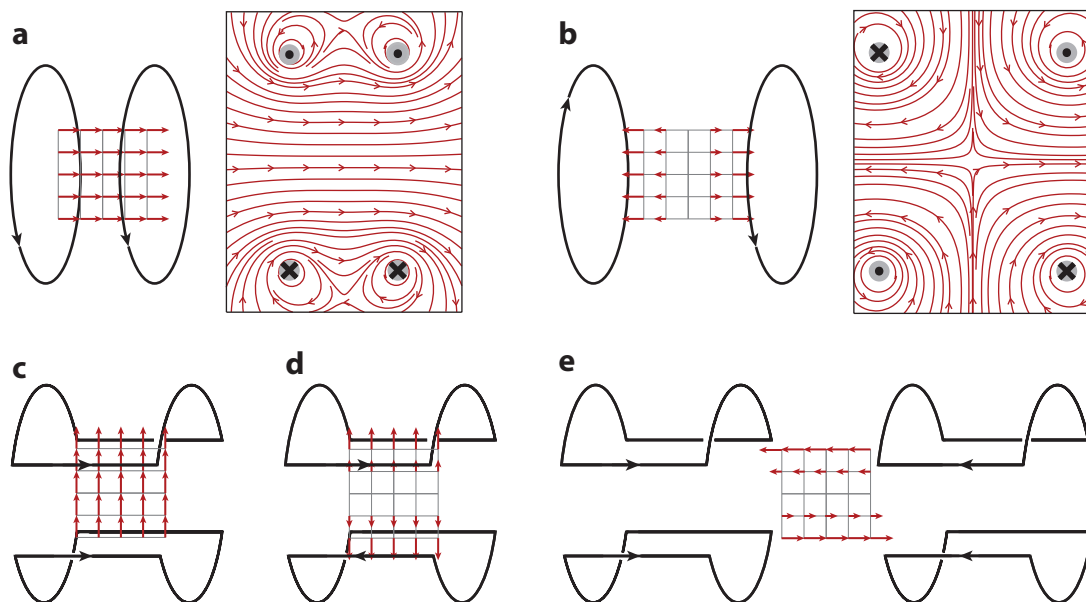


Figure 4

Nominal field approximation in the central workspace of (a) a Helmholtz coil, (b) a Maxwell coil, (c) a uniform saddle coil, (d) a gradient saddle coil, and (e) a double-saddle Golay coil. Arrowheads indicate the direction of current flow in the coils associated with the field shown. For the Helmholtz and Maxwell coils, the actual radially symmetric field streamlines are also shown.

workspace rather than focusing entirely on the common center. A Helmholtz coil can be used to generate an essentially force-free torque on a magnetic object.

If we return to our set of two coaxial circular coils of equal radius r , but instead source the current through the coils with opposite handedness, we find that the fields perfectly cancel to $\|\mathbf{b}\| = 0$ at the common center, but the spatial derivative of the field in the common center is not zero. A Maxwell coil is such an arrangement in which the separation distance between the coils is $\sqrt{3}r$ (Figure 4b), which is optimal in the sense that the second derivative of the field in the axial z direction is zero, creating a so-called uniform gradient. The nominal field derivative in the axial z direction is $\partial b_z / \partial z = (0.64\mu_0/r^2)i$. A Maxwell coil can be used to generate an essentially torque-free force on a magnetic object.

Saddle coils get their name from their characteristic shape, with their geometry constrained to the surface of a cylinder. Saddle coils can be optimized to generate a uniform field (Figure 4c) or a gradient field (Figure 4d) orthogonal to the axis of the cylinder (29). Double-saddle Golay coils (Figure 4e) create a transverse gradient (30). Saddle coils can be combined with Helmholtz and Maxwell coils to facilitate a cylindrical workspace with access from the ends of the cylinder.

The most common use of Helmholtz coils in robotics is the arrangement of two or three mutually orthogonal nested sets of coils (31). Each Helmholtz coil generates a uniform field aligned with a basis direction, and by controlling the independent currents, one can create a uniform field in the common center with controllable direction and magnitude. The parametric design of triaxial Helmholtz coils, both circular and square, is provided in Reference 32. Incorporating a single Maxwell coil into a triaxial Helmholtz coil provides some additional manipulation capability (33, 34).

The clinical MRI scanner is the most notable system utilizing the specialized coils described above. It has potential for biomedical robotics, not least because MRI scanners are already available in hospitals. Unlike other magnetic-actuation systems, an MRI scanner cannot modify the strong uniform z -axis bore field produced by its main superconducting magnets. The bore field of several teslas in an MRI scanner is significantly larger than the field created by other systems, and thus magnetic materials are typically treated as saturated in the scanner, with magnetization aligning with the scanner's bore field. The scanner incorporates a Maxwell coil ($\partial b_z / \partial z$) and two Golay coils ($\partial b_z / \partial x$ and $\partial b_z / \partial y$) that enable spatial changes in the field magnitude (but not direction), as well as radio-frequency electromagnetic coils used for imaging. Section 8.2.2 describes applications of the MRI scanner.

Even coils without the optimal designs described above will exhibit a similar field-generation capability and may be required as a design compromise. For example, six independent coils arranged on the face of a cube (like three orthogonal pairs) will result in a system with similar capabilities to a triaxial Helmholtz–Maxwell system (35, 36). A system designed for capsule endoscopy utilized 12 independent coils arranged as six pairs, with the ability to set all independent field and field-derivative components (37).

5.3. Magnetically Nonorthogonal Systems of Electromagnets

In recent years, there has been a move away from magnetically orthogonal systems to systems of electromagnets that surround a workspace and work together in a coupled fashion, where all electromagnets are active for all actuation commands in general. This design philosophy is less constraining on the size and shapes of workspaces that can be created.

A variety of systems have been designed to surround the workspace with configurations of eight electromagnets arranged such that their respective axes all pass through a common point in the center of the workspace (which is an arbitrary constraint). Each of these configurations is capable

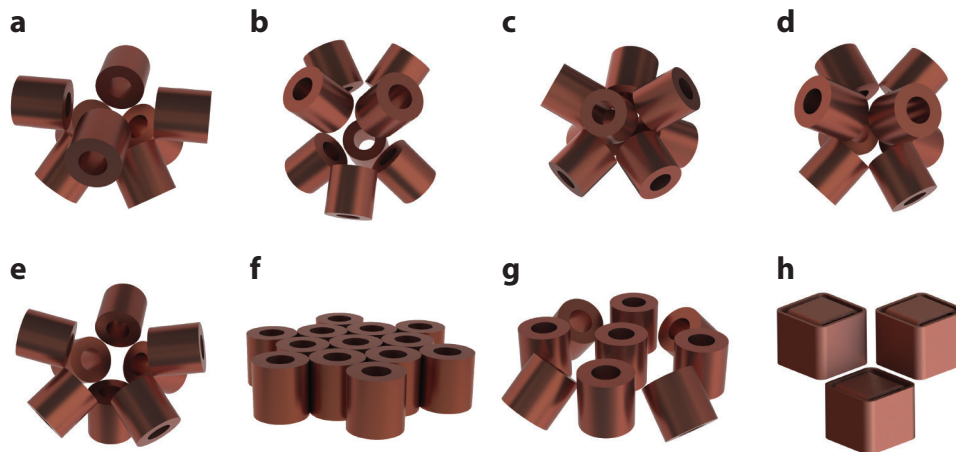


Figure 5

Electromagnet configurations: (a) OctoMag; (b) 45° - 45° - 45° ; (c) square antiprism; (d) cubic; (e) open asymmetric; (f) parallel planar array, shown here with 13 magnets; (g) 9-magnet planar array; (h) Omnimagets, shown here with 3 Omnimagets (and thus 9 electromagnets).

of full eight-DOF field generation. The first such configuration was the OctoMag (27), which had a set of four electromagnets oriented 90° from a central axis (i.e., in a plane) and another set of four electromagnets oriented 45° from the central axis, with the two sets rotated 45° from each other about the central axis (**Figure 5a**). Variants on the OctoMag configuration are described in References 38–40. A departure from the OctoMag (**Figure 5b**) oriented the electromagnets that were in the planar set such that they were 45° from the central axis (41). A variant on this idea (**Figure 5c**), introduced in Reference 42 and dubbed the square antiprism in Reference 43, oriented the electromagnets 60° from the central axis; this is the eight-electromagnet configuration for which the magnets are maximally separated and thus maximally independent (43). Another configuration, employed by the company Magnetecs (44), has electromagnets on each of the eight corners of a cube (**Figure 5d**). A critical comparison of a subset of the above eight-electromagnet configurations was performed in Reference 43, which quantified the trade-off between field (torque) generation, field-derivative (force) generation, and access to the workspace. Each of the configurations described above shows a high degree of symmetry about a central axis of the workspace. The need for such symmetry was critically questioned in Reference 43, which introduced an open-asymmetric configuration (**Figure 5e**) that has substantially improved access to the workspace without a substantial loss in the system's field-generation capability.

A number of systems have been described that use more than eight electromagnets, creating a degree of redundancy. One such concept comprises an arbitrary number of parallel electromagnets arranged in a plane with a hexagonal packing (**Figure 5f**), creating a workspace that is scalable in the planar direction (45) but relatively shallow in the direction orthogonal to that plane. The electromagnets can also be arranged with a square packing (46), but hexagonal packing has a higher packing density. A related nonmodular system concept (47) uses exactly nine electromagnets in a 3×3 planar array, with four of the outer electromagnets rotated to point toward a common central workspace (**Figure 5g**).

Another modular concept involves Omnimagets (48). An Omnimagnet is a cubic device comprising three nested mutually orthogonal coils with an optional spherical ferromagnetic core at the center, which was optimized to be well modeled by the dipole model of Equation 3.

Although it is possible to utilize a single Omnimagnet as a manipulation or actuation source (49), Omnimagnets were developed for use in modular and reconfigurable systems, with n Omnimagnets providing $3n$ independent electromagnets (50). Although Omnimagnets may still surround a system workspace (**Figure 5b**), the axes of the individual electromagnets are no longer all pointing toward the workspace.

5.4. Electromagnet Design

Electromagnets are typically designed as insulated copper wire (i.e., magnet wire) wrapped around a ferromagnetic core, which serves to amplify the field. The core is typically made of an ideal soft-magnetic material to avoid effects of hysteresis. In some cases, the core extends beyond the coil, typically to enable the relatively small-diameter core to get closer to the workspace while keeping the relatively large-diameter coils at a distance. In some cases, the electromagnet (either the coil or the core) is tapered, also with the goal of getting closer to the workspace. To date, designing ferromagnetic-core electromagnets has been an iterative process, relying heavily on FEA methods. However, a few sources have shed some light on design trade-offs (38, 51–53).

Shaping the tips of electromagnetic cores can result in further focus of the magnetic field, which leads to stronger gradients in a small workspace (38, 54). An extreme version of tip shaping is seen in magnetic tweezers, in which fine-tip cores are used for micro- or nanomanipulation in an optical microscope (18, 55, 56). If the goal of the design is to achieve the maximum magnetic field and/or gradient in a small space, then all of the flux from the generating magnets should be focused into the workspace using a soft-magnetic yoke that forms a closed magnetic circuit with a small gap, which is the workspace (57, 58). Yoke-based systems can achieve fields up to 1 T in strength for small gap sizes but are sometimes limited in workspace size and ability to generate fields and gradient forces in an arbitrary direction.

Electromagnets can also be designed without any core, which is sometimes referred to as having an air core. The benefits of such a design choice are that the field of an individual electromagnet can be computed simply using the methods of Section 2.3 and that multiple electromagnets are quasi-statically decoupled from each other (which is particularly desirable in systems of moving electromagnets). The optimal design of coreless electromagnets, in terms of maximizing field strength at a given point, is known (59); however, when constrained to a (tapered) cylindrical volume, the optimal design is less than 1% better than the best (tapered) cylindrical design. Coreless electromagnets are rarely used because it is typically assumed that cores will enable stronger systems. If the object being manipulated or actuated is small relative to the workspace, such that it is many of its own body lengths away from the cores, this assumption is likely correct. However, as objects become larger, their self-attraction to the cores can make cores undesirable (60).

It is common to include a cooling system to mitigate resistive heating in electromagnets (27). However, the effectiveness of cooling systems is ultimately limited by the coolant-coil heat-exchange area and the coolant's temperature. Cooling with liquid nitrogen, for example, both increases this temperature differential and substantially reduces the coil resistance, enabling larger currents to be sourced through the coils without overheating (61). Superconducting electromagnets, which do not have resistive losses and can sustain a higher current density than typical electromagnets, have also been explored for manipulation systems (62). These systems require cryogenic cooling, which raises potential safety concerns if the cooling cannot be maintained and the magnets quench (i.e., transition to nonsuperconducting). Care must be also taken when designing strong superconducting magnets to consider the material's maximum current density, maximum current slew rate, and maximum transverse magnetic field, as these factors can initiate a quench.

6. MOVING SYSTEMS FOR MANIPULATION AND ACTUATION

6.1. Moving Permanent Magnets

Permanent magnets can generate strong fields—with no electrical currents or the associated generation of heat—which can be controlled by translating and/or rotating these sources. Although the effects of translation and rotation on the field and field derivative are nonlinear, control of these systems can be achieved using nonlinear solution methods. These sources are commonly modeled as point dipoles, which is quite accurate even for nonspherical magnets as long as the interaction distances exceed two minimum-bounding-sphere radii (4). If closer distances are required, more complex field models can be employed. Because their magnetization is not sensitive to the field they experience, superposition applies and each source can be treated independently. Thus, the field and its gradient at location \mathbf{P}_b from n actuating permanent magnets are the summation of all of the individual contributions:

$$\mathbf{b}(\mathbf{P}_b) = \sum_{i=1}^n \mathbf{b}(\mathbf{P}_b, \mathbf{m}_i, \mathbf{P}_i), \quad G(\mathbf{P}_b) = \sum_{i=1}^n G(\mathbf{P}_b, \mathbf{m}_i, \mathbf{P}_i), \quad F(\mathbf{P}_b) = \begin{bmatrix} \mathbf{b}(\mathbf{P}_b) \\ G(\mathbf{P}_b) \end{bmatrix}. \quad 28.$$

The force and torque on an object at position \mathbf{P}_b follow directly from Section 4.

A general actuation system using permanent magnets would move the six-DOF pose of each actuating magnet. Thus, each actuating magnet's motion can provide up to six field-array inputs, with radially symmetric fields (e.g., spheres and axially magnetized cylinders) providing only five. However, the ability to fully control the poses of the magnets will be mediated by the robotic positioning system, parameterized by the array Q (e.g., the positioning robot's joint angles). These relationships are nonlinear, so solutions are typically framed as a control or optimization problem (63–65), analogous to Equation 27:

$$\dot{Y} = \mathbb{J}_{YQ}(\mathbf{m}, \mathbf{P}_b, Q) \dot{Q} = \left(\mathbb{M}_Y(\mathbf{m}) + \left[\frac{\partial \mathbb{M}_Y(\mathbf{m})}{\partial F(1)} F \cdots \frac{\partial \mathbb{M}_Y(\mathbf{m})}{\partial F(8)} F \right] \right) \mathbb{J}_{FX}(\mathbf{P}_b, Q) \mathbb{J}_{XQ}(Q) \dot{Q}, \quad 29.$$

where $\mathbb{J}_{XQ}(Q)$ is the positioning robot's velocity Jacobian that maps the joint velocities to the six-DOF velocities of the magnet(s), and $\mathbb{J}_{FX}(\mathbf{P}_b, Q)$ is a Jacobian that relates the magnet velocities to changes in the field array. The actuating magnet or magnets are driven in the direction that reduces the error between the actual and desired output Y . To maintain control, care must be taken to keep the Jacobian \mathbb{J}_{YQ} full rank, which is a necessary condition (22).

Several special cases have been implemented. The first is the use of a single actuating magnet, mounted on a six-DOF robotic arm such that its full position and orientation can be controlled within the workspace of the robot arm (63, 66). This approach creates a very large actuation workspace that is limited only by the reach of the robot arm and leaves the workspace relatively unobstructed. However, the method relies on gravity for downward motions of the manipulated object. A second approach is to constrain individual actuating magnets to each rotate about a single axis. This has been done with eight actuating magnets arranged around the workspace (64). This approach has the advantages that it uses a system with no translating parts and can generate a more uniform field than a single movable source can.

Other hybrid approaches are possible as well. The Stereotaxis Niobe system consists of two very large permanent magnets with a workspace in between, where each magnet can translate and rotate within a constrained range to ensure safety and usability in a clinical environment (67). This system is used to create uniform fields for catheter steering and can create large field strength. Many variations with coupled rotations of permanent magnets have also been shown, which can generate relatively large fields but have a reduced ability to create arbitrary fields and

field gradients (68). Other systems have been created for manipulation on 2-D surfaces (69) or to locally repel microparticles (see Reference 19 and references therein).

6.2. Moving Electromagnets

Electromagnets can also be moved through space to vary magnetic inputs to a robotic system. Nonlinear methods still apply, with I and Q as the complete input set:

$$\dot{Y} = \left(\mathbb{M}_Y\{\mathbf{m}\} + \left[\frac{\partial \mathbb{M}_Y\{\mathbf{m}\}}{\partial F(1)} F \dots \frac{\partial \mathbb{M}_Y\{\mathbf{m}\}}{\partial F(8)} F \right] \right) \left(\mathbb{F}_I\{\mathbf{P}_b, Q\} \dot{I} + \mathbb{J}_{FX}\{\mathbf{P}_b, Q, I\} \mathbb{J}_{XQ}\{Q\} \dot{Q} \right). \quad 30.$$

The \dot{F} term is the summation of the analogous terms from Equations 27 and 29 but with a configuration-dependent coupling between the two field Jacobians. Calculating these coupled Jacobians is generally not trivial for systems with soft-magnetic coupling (e.g., ferromagnetic cores) but can be straightforward for coreless systems because the fields generated by the individual coils are independent.

A variety of systems have combined the specialized coils of Section 5.2, in various arrangements, with the capability to move one or more of the coils in order to increase the DOFs of control. A pioneering work in magnetic methods in robotics utilized this strategy by combining a Helmholtz and Maxwell coil coaxially and then robotically rotating that system (70). Others have expanded on that concept with additional DOFs of control (71, 72).

Other systems are more reminiscent of those in Section 5.3. Four air-core electromagnets have been mounted on robotic positioning arms for medical use (73). The BigMag system comprises two sets of three electromagnets, with each set capable of one-DOF rotation (74). The DeltaMag system comprises three electromagnets, each of which can rotate about a single axis (75). These concepts yield larger, more open workspaces than would be possible with equivalent stationary systems.

Because the average applied field over any spherical volume is equal to the applied field at the center of that spherical volume (3), it is possible to approximate the magnetization of a soft-magnetic sphere using knowledge of the applied field at only a single point. This was described in the context of systems of Omnimagets in Reference 50, which provided an algebraic (approximate) solution for the coupled field of multiple Omnimagets. In Omnimagets, the locations of the spherical cores coincide with the locations of the three coils of the respective Omnimagets, but the methodology will work for soft-magnetic spheres in any location with respect to the field-generation system.

7. SYSTEM CHARACTERIZATION AND CALIBRATION

The methods and analysis described in the previous sections assume an accurate understanding of the field generated by the system, which can be achieved through either characterization (i.e., field mapping) or calibration (i.e., fitting parameters to a structured model). For stationary electromagnet systems, with or without soft-magnetic coupling, field maps or models are generated in the workspace frame with all electromagnets in situ. We first address this special case and then discuss movable sources.

Characterization relies on field measurements, with no physics-based model. Measurements of the field contribution from each coil are obtained from either FEA simulations or direct experimental measurements. The field data are recorded in a lookup table and are later interpolated using standard methods, such as trilinear or tricubic interpolation, to extract the field and field derivative at a point (35, 45, 57, 76–78). B-splines have also been suggested as a convenient way

of interpolating the measured data while providing some filtering capabilities (79). Each interpolation model is used to fill in a column of the \mathbb{B} matrix described in Equation 23 when applying a unit current. Although characterization methods have been applied successfully in the literature, they cannot detect and correct for uncertainties in the sensor readings, orientations, or locations. Furthermore, since only magnetic-field (not field-derivative) sensors are presently available, the numerical differentiation used to calculate the field-derivative matrix \mathbb{B}_∇ (and associated G) results in values that do not conform to Maxwell's equations (i.e., Equations 1 and 2). Success using characterization methods is due primarily to the robustness of feedback control.

Calibration of a magnetic system does not share the limitations of characterization, as it fits a physics-based model of the field to the data collected (47, 80). Model-based calibration works by approximating each field source with a single- or multipole expansion of a field source (see Equation 5), where the calibration process defines the locations, orientations, and strengths of each source. When implementing such an approach, care should be taken to identify all magnetic sources. For example, in a system with eight ferromagnetic-core electromagnets, each current input magnetizes each of the cores differently; thus, the system should consider potentially 64 sources. A model comprising only dipole-field (single-pole) terms, with fewer sources considered than the ideal described above, is often sufficient (27, 63, 81). However, including all potential sources, as well as the first three terms in the multipole expansion, results in less than 1% error in practice (80). The basic procedure is as follows. Given a system with n_c current inputs associated with n_s magnetic source locations, a set of $n_c \times n_s$ dipole sources, located at positions $\mathbf{P}_{i,j}$ with unit-current source strengths $\mathbf{m}_{i,j}$ associated with $I(i) = 1$ A, are used to model the field in the workspace. For a given field measurement \mathbf{b}_k at location \mathbf{P}_k , taken with input current array I_k , the expected field measurement is

$$\tilde{\mathbf{b}}_k = \mathbf{b}_e + \sum_{i=1}^{n_c} \sum_{j=1}^{n_s} \mathbf{b}(\mathbf{P}_k, \mathbf{m}_{i,j} I_k(i), \mathbf{P}_{i,j}), \quad 31.$$

where \mathbf{b}_e is a constant background term (e.g., Earth's field). Given n_m field measurements \mathbf{b}_k , the calibration process finds the set of unit-current source strengths $\mathbf{m}_{i,j}$ and source locations $\mathbf{P}_{i,j}$, as well as the background field, to satisfy the minimization problem

$$\arg \min_{\mathbf{m}_{i,j}, \mathbf{P}_{i,j}, \mathbf{b}_e} \sum_{k=1}^{n_m} \|\mathbf{b}_k - \tilde{\mathbf{b}}_k\|^2, \quad 32.$$

which can be solved using interior-point methods (47) or nonlinear programming (80). Because the dipole fields are nonlinear with respect to the optimization variables, there are multiple solutions to this nonconvex optimization problem. Consequently, a good initial guess of field source position and orientation is necessary to achieve a reasonably optimal solution. In addition, care should be taken to verify that the solution does not result in sources located within the workspace, as such a solution would lead to infinite-magnitude field estimates at these locations. If this happens, the optimization should be run with a different initial guess, possibly with additional constraints or a different number of sources.

Both the characterization and calibration approaches discussed above were presented for the special case of stationary electromagnetic sources, with any soft-magnetic components below saturation. For movable magnetic sources, including permanent magnets and coreless electromagnets, field maps or models are generated in each individual source's coordinate frame, using an appropriate simplification of Equation 31: For coreless electromagnets, $n_s = 1$; for permanent magnets, $\mathbf{m}_{i,j}$ are the source strengths, with no notion of current. The field maps or models are then transformed to the workspace frame when implemented in the system. The

field transforms as a standard vector ${}^w\mathbf{b} = {}^w\mathbb{R}_s {}^s\mathbf{b}$, whereas ${}^s\mathbb{B}_\nabla \equiv [\frac{\partial {}^s\mathbf{b}}{\partial x} \quad \frac{\partial {}^s\mathbf{b}}{\partial y} \quad \frac{\partial {}^s\mathbf{b}}{\partial z}]$ transforms as a rank-2 tensor ${}^w\mathbb{B}_\nabla = {}^w\mathbb{R}_s {}^s\mathbb{B}_\nabla {}^w\mathbb{R}_s^\top$. Movable sources with soft-magnetic coupling will require more elaborate methods.

8. EXTENSIONS AND APPLICATIONS

8.1. Extensions

Here we describe two extensions to the basic methods described above, which have the potential to be applied in a variety of applications.

8.1.1. Rotating fields. We introduced the triaxial Helmholtz coil in Section 5.2 as a means of generating controllable uniform fields. The most common use of such a system is to generate rotating fields. This has been particularly important for the actuation of microrobots that transduce the rotating field into rolling, swimming, or screwing, as the microrobots experience a force-free torque that attempts to align their magnetic components with the field (31). It is possible to generate a locally uniform field using other electromagnetic systems by setting the desired field gradient to $G = 0_{5 \times 1}$. Alternatively, superimposing a strong gradient field can effectively lock the surrounding workspace while leaving a selected location free for rotation (36).

When a magnetic dipole is rotated about (and orthogonal to) an axis, the magnetic-field vector at each location in space also rotates about (and is orthogonal to) some axis. Reference 81 showed that this problem is always invertible: Given a desired field-rotation axis at a given position, the necessary dipole-rotation axis can be computed. This method can be used to generate rotating fields that can be used for actuation. The fields are nonuniform and thus not force free in general, and both the magnitude and angular velocity of the field vary throughout each rotation cycle. However, this method enables the field source to be adjacent to the workspace rather than surrounding it. Both electromagnetic (48) and permanent-magnet (82) field sources have been developed to generate continuously rotating dipole fields. Combining multiple rotating dipole fields can generate rotating fields that are more uniform (83).

8.1.2. Multi-degree-of-freedom magnetic mechanisms. By utilizing multiple constrained magnet dipoles in one robotic device, many degrees of freedom can be controlled. If we assume that the robotic device is small relative to the size of the field-generation source, then all of the dipoles experience approximately the same field and gradients. In this case, there are eight independent components of the field array F that can be exploited for control. If multiple dipoles in the robotic device have distinct magnetization directions, they will each experience different (but potentially coupled) magnetic force and torque in response to these eight inputs. Proper design to achieve a full-rank actuation matrix can enable up to eight-DOF actuation (40).

8.2. Applications

The vast majority of prior work in magnetic methods in robotics has been applied in two areas (and often their intersection): microrobotics and medical robotics.

8.2.1. Microrobotics. Magnetic manipulation is commonly used in the actuation of microrobots, often under the guidance of an optical microscope and for in vivo medical applications. This work typically takes the form of transducing the magnetic forces and torques into a secondary propulsion mechanism (rolling, chiral or helical swimming, wiggling, vibrating, etc.). Both soft and hard magnets are utilized in microrobotics applications. Application of control techniques

to single- and multiagent microrobotic systems has been a major focus area. Although there are other methods of actuating microrobots—such as acoustic, optical, and chemical or biohybrid methods—magnetic actuation is perhaps the most commonly used because of the excellent capability for precise wireless actuation and limited need for the fabrication of complex microdevices. The design and control of microrobots actuated by magnetic fields are subject to microscale physical forces; microrobots exist in an environment that is stochastic and has high viscosity, dominated by surface forces such as friction and adhesion. Numerous survey papers (84–87) and even a textbook (88) have reviewed the use of magnetic methods in microrobotics, so we refer the reader to those sources.

Much recent activity has been in the area of multi-microrobot control using magnetic fields (89). Small groups of microrobots can be independently controlled by utilizing nonlinear magnetic effects (7), fluidic drag (90, 91), interagent magnetic forces (92), and nonuniform magnetic fields (52). Other recent work has been in the area of swarm control of large numbers of micrometer or smaller particles. Groups of micro- or nanoparticles will form long chains due to magnetic attraction, and without control, these chains form randomly and make it difficult to create coordinated motions. However, magnetic microparticles can be aggregated into swarms by careful use of rotating magnetic fields (93–95) that can create reconfigurable shapes suitable for manipulating objects or squeezing through tight areas.

Other main current research topics in the microrobotics area are in localization and feedback using medical imaging (including MRI, ultrasound, and, more recently, magnetic particle imaging), control of microrobotic swarms for targeted drug delivery, the development of biomedically safe or degradable magnetic micro- and nanorobots, and the deployment of microrobots for therapy inside the body.

8.2.2. Medical robotics. Magnetic manipulation has been used in medicine since the 1600s (96) but was originally relegated mostly to removing ferrous objects from within the body using lodestones. With today's advances in both magnetic materials and computation, magnetic manipulation in medicine has garnered significant interest (97) and is being investigated for endoscopic inspections, catheter manipulation, and MRI-guided interventions.

8.2.2.1. Capsule endoscopes. Swallowable camera pills, known as capsule endoscopes, are already used clinically, but these are passive devices that are propelled by the gastrointestinal tract. There has been substantial effort to make the capsules active robotic devices to enable improved diagnosis and therapy (98, 99), and much of that effort has involved magnetic methods. Different solutions have focused on individual organs within the gastrointestinal tract—the stomach, the small intestine (i.e., small bowel), and the large intestine (i.e., colon)—but many techniques could be translated to other organs with minimal modifications. In addition, much of the research in this area has addressed (magnetic) localization of the capsule along with magnetic actuation.

Some work aimed at the stomach has assumed that the capsule is in contact with the walls of the stomach or the surface of a fluid filling the stomach. Permanent-magnet systems enabled only orientation control (67), whereas electromagnetic systems enabled full-DOF control (37, 47). Other work has assumed that the capsule is levitating in the fluid (i.e., not in contact) such that its orientation will align open-loop with the applied field; that work used a single large permanent magnet, positioned above the capsule, for control (63). Other work has developed capsules with magnetically actuable mechanisms (100).

For the small intestine, approaches have focused largely on the use of an external screw thread on the capsule, which enables magnetic torque to be transduced to rotation, which is transduced

into forward or backward motion in the lumen (101). Reference 102 and references therein describe the state of the art in the propulsion and localization of magnetic capsules in a lumen using a single rotating permanent magnet and the method of Section 8.1.1.

The work in the large intestine has utilized both magnetic force and torque. In certain cases, the capsule is a true capsule that is completely untethered (66). Other works have considered so-called tethered capsules, which have a tether that enables energy and matter to be transmitted to the capsule, but the primary means for controlling the pose of the capsule is magnetic and not via the tether (65, 103, 104). With a tethered capsule, it cannot be assumed that the capsule will align with the field open-loop (as in Reference 63). To date, rather than modeling the tether, the tether has been treated as a force-torque disturbance on the capsule that is addressed with closed-loop control.

8.2.2.2. Catheters and other continuum devices. Flexible magnetically guided instruments have been used in medicine since the 1950s (105). Initial developments focused on steel-tipped devices guided using movable magnetic sources to access difficult-to-reach regions of the vasculature and brain (96, 106). It was shown that such devices could be designed and controlled to locomote through both large and small lumens by setting up a swimming-like motion (107). Using these techniques, clinical experiments were performed for navigating the bronchus (108), performing cerebral catheterization for targeted delivery of cytotoxic drugs (109), and making intracranial EEG recordings (110). Since these initial efforts, control of magnetic continuum devices has branched into two areas: catheter-like devices and steerable-needle devices.

Magnetic catheters have received the most attention and are in clinical use (111, 112). Other devices, such as magnetically guided cochlear-implant electrode arrays (113) and endolaser probes (114), have similar mechanics. Manipulation of these devices relies on the interaction between the magnetically induced force and torque and the internal stress to stabilize the system. Treated in its full form, this multiphysics problem becomes nonlinear and is most accurately treated using FEA, which can be used to characterize and control the system by constructing a data-driven predictive model for use in a feedback loop (115). However, much can be accomplished with increasingly complex approximations to the full model. The first approach, which assumes no knowledge of the magnetic system or elastic properties, learns the local mapping between the system inputs and resulting device motions directly from the captured endoscopic image (39). If localization is available, the most easily implemented approach is to treat the interaction between the magnetic element and the elastic element as an unmodeled disturbance and use the same control approaches discussed above for untethered systems (65, 103, 116). This method relies on the robustness of the feedback control system to correct for the elastic disturbance to the system and is effective in many situations. If the tether is highly flexible but not extensible, then its effect on the magnetic components can be accounted for as a position constraint, while the closed-loop controller can correct for the minor elastic effects (117).

For systems in which the elastic effects cannot be ignored, but the deflections are small and the magnetic field is fairly uniform, Euler–Bernoulli beam theory can be used to predict the deflections and create a Jacobian-based controller to step the continuum device from one equilibrium configuration to another (118–120). Another approach, which can handle larger deformations but simplifies the continuum-mechanics modeling, is to represent the continuum magnetic device as a series of elastic joints connected by rigid segments (121, 122). If the magnetic fields are uniform and the continuum device deflects with constant curvature, then a geometrically exact and closed-form model that can handle large deformations can be created using Kirchhoff elastic rod theory (114, 123–125). Finally, Cosserat elastic rod theory can be used to numerically model and control magnetic continuum devices with heterogeneous constructions and large deformations in

a nonuniform magnetic field efficiently with minimal approximations (126, 127). One advantage of this approach is that it can predict and avoid complex nonlinear behaviors, such as solution bifurcations, that may become problematic for the control schemes discussed (127, 128). Each of these approaches incrementally steps from one stable configuration to another and ignores the dynamics that realize this change. A dynamic treatment of magnetic continuum devices and control systems that can adjust these dynamics is an open research area.

Steerable-needle devices, which have received relatively less attention in the magnetic-actuation literature, rely on interactions with tissue to create mechanical deformations in their shape. Both soft-magnetic (129) and permanent-magnet (130) tips have been explored. These devices use magnetic torque to deflect the tip to be out of alignment with the current trajectory. The asymmetric forces between the tip and the surrounding tissues cause the device to deflect upon insertion, enabling precise device trajectories.

8.2.2.3. MRI scanner. We introduced the use of a clinical MRI scanner as a magnetic-manipulation system in Section 5.2. Clinical MRI scanners, with minor hardware and software modifications, have been used for actuation of micrometer- to centimeter-size magnetic objects, with the gradient coils used to create forces on magnetic objects (131–133). Imaging can be time-multiplexed with the actuation to leverage the MRI imaging for real-time feedback (albeit at relatively slow feedback rates). Magnetic particles can be moved against blood flow, with the potential for targeted drug delivery (134). Robotic mechanisms can be driven wirelessly (135, 136) for applications such as needle insertion. Active magnetic catheters can capitalize on the strong bore field (120, 122). Another use of this uniform field is to introduce large soft-magnetic spheres into the scanner, which severely distort the field and create field gradients (137); by manipulating the position of these spheres, these field gradients can be used for robotic manipulation of other objects. It is sometimes possible to leverage the magnetic-actuation hardware to also enable magnetic localization of the medical device being controlled (138).

8.2.3. Other areas. Compared with microrobotics and medical robotics, other areas have received relatively limited attention but highlight the potential broad applicability of magnetic methods in robotics.

8.2.3.1. Untethered magnetic haptic interfaces. The techniques developed for magnetic manipulation can be applied in the context of untethered magnetic haptic interfaces (UMHIs), in which a magnetic object is attached to a tool (e.g., stylus) or directly to the body (e.g., a fingertip). UMHIs eliminate the need for a mechanical linkage, with its associated inertia and friction. They differ substantially from Lorentz-force (maglev) haptic interfaces, which in many aspects of construction and control are more similar to electromagnetic machines (e.g., motors) than to the types of systems discussed in this article. UMHIs based on planar coils (e.g., **Figure 5f**) have been the most explored to date (45, 46, 139, 140). The open-asymmetric design shown in **Figure 5e** was also motivated by its use as a UMH. There is evidence that UMHIs may substantially reduce the instability typically associated with the rendering of stiff haptic virtual walls (60). In addition to kinesthetic (i.e., quasi-static) rendering, high-frequency sensations can be rendered (139–141), including force-torque illusions.

8.2.3.2. Aerospace systems. One of the earliest uses of the methods described in this article was active control of an aircraft within a wind tunnel (142, 143). A sphere rigidly embedded in an airframe model enabled its support in a wind tunnel with no mechanical attachments that would disturb the airflow. The control inputs also enabled the estimation of drag forces on the model.

Finally, there is a body of literature focused on techniques to enable coordinated control of modular and fractionated spacecraft, known as electromagnetic formation flight (see Reference 144 and references therein). Each spacecraft is assumed to have three orthogonal electromagnetic coils to generate controllable magnetic dipoles, which are used to control the relative positions of the spacecraft via dipole–dipole interactions.

9. CONCLUSIONS

This article has provided an introduction to the use of magnetic methods in robotics. Although our terminology and magnetic-modeling approach may differ from those of other works, we have striven to introduce the reader to a consistent way of thinking about magnetic systems that can be used to study nearly all magnetically actuated robotics problems. As much as possible, we have connected these concepts to core concepts in robotic manipulation to enable the reader to leverage the wealth of knowledge concerning the mathematics of robotics.

DISCLOSURE STATEMENT

The authors hold patents related to magnetic methods and devices.

ACKNOWLEDGMENTS

We would like to thank Adam J. Sperry for creating **Figure 2** and Ashkan Pourkand for creating **Figure 5**. We would also like to thank Dr. Bradley J. Nelson and Dr. Metin Sitti, because it was through their vision and support that we roboticists became “magneticians.”

LITERATURE CITED

1. Lynch KM, Park FC. 2017. *Modern Robotics: Mechanics, Planning, and Control*. Cambridge, UK: Cambridge Univ. Press
2. Furlani EP. 2001. *Permanent Magnet and Electromechanical Devices*. San Diego, CA: Academic
3. Griffiths DJ. 1999. *Introduction to Electrodynamics*. Upper Saddle River, NJ: Prentice Hall
4. Petruska AJ, Abbott JJ. 2013. Optimal permanent-magnet geometries for dipole field approximation. *IEEE Trans. Magn.* 49:811–19
5. Cullity BD, Graham CD. 2009. *Introduction to Magnetic Materials*. Piscataway, NJ: IEEE Press. 2nd ed.
6. Liorzou F, Phelps B, Atherton DL. 2000. Macroscopic models of magnetization. *IEEE Trans. Magn.* 36:418–28
7. Diller E, Zhang N, Sitti M. 2013. Modular micro-robotic assembly through magnetic actuation and thermal bonding. *J. Micro-Bio Robot.* 8:121–31
8. Abbott JJ, Ergeneman O, Kummer MP, Hirt AM, Nelson BJ. 2007. Modeling magnetic torque and force for controlled manipulation of soft-magnetic bodies. *IEEE Trans. Robot.* 23:1247–52
9. Osborn JA. 1945. Demagnetizing factors of the general ellipsoid. *Phys. Rev.* 67:351–57
10. Chen DX, Pardo E, Sanchez A. 2002. Demagnetizing factors of rectangular prisms and ellipsoids. *IEEE Trans. Magn.* 38:1742–52
11. Joseph RI, Schlömann E. 1965. Demagnetizing field in nonellipsoidal bodies. *J. Appl. Phys.* 36:1579–93
12. Chen DX, Brug JA, Goldfarb RB. 1991. Demagnetizing factors for cylinders. *IEEE Trans. Magn.* 27:3601–19
13. Beleggia M, De Graef M, Millev YT. 2006. The equivalent ellipsoid of a magnetized body. *J. Phys. D* 39:891–99
14. Beleggia M, Vokoun D, De Graef M. 2009. Demagnetization factors for cylindrical shells and related shapes. *J. Magn. Mater.* 321:1306–15
15. Aharoni A. 1998. Demagnetizing factors for rectangular ferromagnetic prisms. *J. Appl. Phys.* 83:3432–34

16. Hagedorn FB, Gyorgy EM. 1968. Magnetic-shape anisotropy in polygonal prisms. *J. Appl. Phys.* 39:995–97
17. Martel S. 2015. Magnetic nanoparticles in medical nanorobotics. *J. Nanopart. Res.* 17:75
18. Wang X, Ho C, Tsatskis Y, Law J, Zhang Z, et al. 2019. Intracellular manipulation and measurement with multipole magnetic tweezers. *Sci. Robot.* 4:eaav6180
19. Shapiro B, Kulkarni S, Nacev A, Sarwar A, Preciado D, Depireux DA. 2014. Shaping magnetic fields to direct therapy to ears and eyes. *Annu. Rev. Biomed. Eng.* 16:455–81
20. Cheang UK, Roy D, Lee JH, Kim MJ. 2010. Fabrication and magnetic control of bacteria-inspired robotic microswimmers. *Appl. Phys. Lett.* 97:213704
21. Beleggia M, Tandon S, Zhu Y, De Graef M. 2004. On the computation of the demagnetization tensor for particles of arbitrary shape. *J. Magn. Mater.* 272–76(Suppl.):E1197–99
22. Petruska AJ, Nelson BJ. 2015. Minimum bounds on the number of electromagnets required for remote magnetic manipulation. *IEEE Trans. Robot.* 31:714–22
23. Giltinan J, Sitti M. 2019. Simultaneous six-degree-of-freedom control of a single-body magnetic micro-robot. *IEEE Robot. Autom. Lett.* 4:508–14
24. Diller E, Giltinan J, Lum GZ, Ye Z, Sitti M. 2016. Six-degree-of-freedom magnetic actuation for wireless microrobotics. *Int. J. Robot. Res.* 35:114–28
25. Thornley CR, Pham LN, Abbott JJ. 2019. Reconsidering six-degree-of-freedom magnetic actuation across scales. *IEEE Robot. Autom. Lett.* 4:2325–32
26. Hsu A, Cowan C, Chu W, McCoy B, Wong-Foy A, et al. 2017. Automated 2D micro-assembly using diamagnetically levitated milli-robots. In *2017 International Conference on Manipulation, Automation, and Robotics at Small Scales*, pp. 160–65. Piscataway, NJ: IEEE
27. Kummer MP, Abbott JJ, Kratochvil BE, Borer R, Sengul A, Nelson BJ. 2010. OctoMag: an electromagnetic system for 5-DOF wireless micromanipulation. *IEEE Trans. Robot.* 26:1006–17
28. Firester AH. 1966. Design of square Helmholtz coil systems. *Rev. Sci. Instrum.* 37:1264–65
29. Ginsberg DM, Melchner MJ. 1970. Optimum geometry of saddle shaped coils for generating a uniform magnetic field. *Rev. Sci. Instrum.* 41:122–23
30. Hidalgo-Tabon SS. 2001. Theory of gradient coil design methods for magnetic resonance imaging. *Concepts Mag. Res. A* 36A:223–42
31. Ishiyama K, Arai KI, Sendoh M, Yamazaki A. 2003. Spiral-type micro-machine for medical applications. *J. Micromechatron.* 2:77–86
32. Abbott JJ. 2015. Parametric design of tri-axial nested Helmholtz coils. *Rev. Sci. Instrum.* 86:054701
33. Ha YH, Han BH, Lee SY. 2010. Magnetic propulsion of a magnetic device using three square-Helmholtz coils and a square-Maxwell coil. *Med. Biol. Eng. Comput.* 48:139–45
34. Choi H, Cha K, Jeong S, Park J, Park S. 2013. 3-D locomotive and drilling microrobot using novel stationary EMA system. *IEEE/ASME Trans. Mechatron.* 18:1221–25
35. Meeker D, Maslen EH, Ritter RC, Creighton F. 1996. Optimal realization of arbitrary forces in a magnetic stereotaxis system. *IEEE Trans. Magn.* 32:320–28
36. Rahmer J, Stehning C, Gleich B. 2017. Spatially selective remote magnetic actuation of identical helical micromachines. *Sci. Robot.* 2:eaal2845
37. Keller H, Juloski A, Kawano H, Bechtold M, Kumura A, et al. 2012. Method for navigation and control of a magnetically guided capsule endoscope in the human stomach. In *2012 4th IEEE RAS and EMBS International Conference on Biomedical Robotics and Biomechatronics*, pp. 859–65. Piscataway, NJ: IEEE
38. Kratochvil BE, Kummer MP, Erni S, Borer R, Frutiger DR, et al. 2014. MiniMag: a hemispherical electromagnetic system for 5-DOF wireless micromanipulation. In *Experimental Robotics*, ed. O Khatib, V Kumar, G Sukhatme, pp. 317–29. Berlin: Springer
39. Edelmann J, Petruska AJ, Nelson BJ. 2018. Estimation-based control of a magnetic endoscope without device localization. *J. Med. Robot. Res.* 3:1850002
40. Salmanipour S, Diller E. 2018. Eight-degrees-of-freedom remote actuation of small magnetic mechanisms. In *2018 IEEE International Conference on Robotics and Automation*, pp. 3608–13. Piscataway, NJ: IEEE

41. Khalil ISM, Magdanz V, Sanchez S, Schmidt OG, Misra S. 2013. Three-dimensional closed-loop control of self-propelled microjets. *Appl. Phys. Lett.* 103:172404
42. Diller E, Sitti M. 2014. Three-dimensional programmable assembly by untethered magnetic robotic micro-grippers. *Adv. Funct. Mater.* 24:4397–404
43. Pourkand A, Abbott JJ. 2018. A critical analysis of eight-electromagnet manipulation systems: the role of electromagnet configuration on strength, isotropy, and access. *IEEE Robot. Autom. Lett.* 3:2957–62. Erratum. 2019. *IEEE Robot. Autom. Lett.* 4:2251
44. Gang ES, Nguyen BL, Shachar Y, Farkas L, Farkas L, et al. 2011. Dynamically shaped magnetic fields initial animal validation of a new remote electrophysiology catheter guidance and control system. *Circ. Arrhythm. Electrophysiol.* 4:770–77
45. Berkelman P, Dzadovsky M. 2013. Magnetic levitation over large translation and rotation ranges in all directions. *IEEE/ASME Trans. Mechatron.* 18:44–52
46. Adel A, Micheal MM, Seif MA, Abdennadher S, Khalil ISM. 2018. Rendering of virtual volumetric shapes using an electromagnetic-based haptic interface. In *2018 IEEE/RSJ International Conference on Intelligent Robots and Systems*, pp. 8737–42. Piscataway, NJ: IEEE
47. Son D, Dong X, Sitti M. 2019. A simultaneous calibration method for magnetic robot localization and actuation systems. *IEEE Trans. Robot.* 35:343–52
48. Petruska AJ, Abbott JJ. 2014. Omnimagnet: an omnidirectional electromagnet for controlled dipole-field generation. *IEEE Trans. Magn.* 50:8400810
49. Petruska AJ, Mahoney AW, Abbott JJ. 2014. Remote manipulation with a stationary computer-controlled magnetic dipole source. *IEEE Trans. Robot.* 30:1222–27
50. Petruska AJ, Brink JB, Abbott JJ. 2015. First demonstration of a modular and reconfigurable magnetic-manipulation system. In *2015 IEEE International Conference on Robotics and Automation*, pp. 149–55. Piscataway, NJ: IEEE
51. Erni S, Schürle S, Fakhraee A, Kratochvil BE, Nelson BJ. 2013. Comparison, optimization, and limitations of magnetic manipulation systems. *J. Micro-Bio Robot.* 8:107–20
52. Ongaro F, Pane S, Scheggi S, Misra S. 2019. Design of an electromagnetic setup for independent three-dimensional control of pairs of identical and nonidentical microrobots. *IEEE Trans. Robot.* 35:174–83
53. Afshar S, Khamesee MB, Khajepour A. 2012. Optimal configuration for electromagnets and coils in magnetic actuators. *IEEE Trans. Magn.* 49:1372–81
54. McCaslin MF. 1958. An improved hand electromagnet for eye surgery. *Trans. Am. Ophthalmol. Soc.* 56:571–605
55. Haber C, Wirtz D. 2000. Magnetic tweezers for DNA micromanipulation. *Rev. Sci. Instrum.* 71:4561–70
56. De Vlaminck I, Dekker C. 2012. Recent advances in magnetic tweezers. *Annu. Rev. Biophys.* 41:453–72
57. Khamesee MB, Kato N, Nomura Y, Nakamura T. 2002. Design and control of a microrobotic system using magnetic levitation. *IEEE/ASME Trans. Mechatron.* 7:1–14
58. Rahmer J, Stehning C, Glech B. 2018. Remote magnetic actuation using a clinical scale system. *PLOS ONE* 13:e0193546
59. Abbott JJ, Osting B. 2018. Optimization of coreless electromagnets to maximize field generation for magnetic manipulation systems. *IEEE Magn. Lett.* 9:1300104
60. Brink JB, Petruska AJ, Johnson DE, Abbott JJ. 2014. Factors affecting the design of untethered magnetic haptic interfaces. In *2014 IEEE Haptics Symposium*, pp. 107–14. Piscataway, NJ: IEEE
61. Leclerc J, Isichei B, Becker AT. 2018. A magnetic manipulator cooled with liquid nitrogen. *IEEE Robot. Autom. Lett.* 3:4367–74
62. Grady MS, Howard MA III, Molloy JA, Ritter RC, Quate EG, Gillies GT. 1990. Nonlinear magnetic stereotaxis: three-dimensional, in vivo remote magnetic manipulation of a small object in canine brain. *Med. Phys.* 17:405–15
63. Mahoney AW, Abbott JJ. 2016. Five-degree-of-freedom manipulation of an untethered magnetic device in fluid using a single permanent magnet with application in stomach capsule endoscopy. *Int. J. Robot. Res.* 35:129–47

64. Ryan P, Diller E. 2017. Magnetic actuation for full dexterity microrobotic control using rotating permanent magnets. *IEEE Trans. Robot.* 33:1398–409
65. Pittiglio G, Barducci L, Martin JW, Norton JC, Avizzano CA. 2019. Magnetic levitation for soft-tethered capsule colonoscopy actuated with a single permanent magnet: a dynamic control approach. *IEEE Robot. Autom. Lett.* 4:1224–31
66. Ciuti G, Valdastrì P, Menciasì A, Dario P. 2010. Robotic magnetic steering and locomotion of capsule endoscope for diagnostic and surgical endoluminal procedures. *Robotica* 28:199–207
67. Carpi F, Pappone C. 2009. Stereotaxis Niobe® magnetic navigation system for endocardial catheter ablation and gastrointestinal capsule endoscopy. *Expert Rev. Med. Devices* 6:487–98
68. Zhang W, Meng Y, Huang P. 2008. A novel method of arraying permanent magnets circumferentially to generate a rotation magnetic field. *IEEE Trans. Magn.* 44:2367–72
69. Zarrouk A, Belharet K, Tahri O, Ferreira A. 2019. A four-magnet system for 2D wireless open-loop control of microrobots. In *2019 International Conference on Robotics and Automation*, pp. 883–88. Piscataway, NJ: IEEE
70. Yesin KB, Vollmers K, Nelson B. 2006. Modeling and control of untethered biomicrorobots in a fluidic environment using electromagnetic fields. *Int. J. Robot. Res.* 25:527–36
71. Jeong S, Choi H, Choi J, Yu C, Park J, Park S. 2010. Novel electromagnetic actuation (EMA) method for 3-dimensional locomotion of intravascular microrobot. *Sens. Actuators A* 157:118–25
72. Choi H, Cha K, Choi J, Jeong S, Jeon S, et al. 2010. EMA system with gradient and uniform saddle coils for 3D locomotion of microrobot. *Sens. Actuators A* 163:410–17
73. Véron B, Hubert A, Abadie J, Andreff N. 2013. Geometric analysis of the singularities of a magnetic manipulation system with several mobile coils. In *2013 IEEE/RSJ International Conference on Intelligent Robots and Systems*, pp. 4996–5001. Piscataway, NJ: IEEE
74. Sikorski J, Denasi A, Bucchi G, Scheggi S, Misra S. 2019. Vision-based 3-D control of magnetically actuated catheter using BigMag—an array of mobile electromagnetic coils. *IEEE/ASME Trans. Mechatron.* 24:505–16
75. Yang L, Du X, Yu E, Jin D, Zhang L. 2019. DeltaMag: an electromagnetic manipulation system with parallel mobile coils. In *2019 International Conference on Robotics and Automation*, pp. 9814–20. Piscataway, NJ: IEEE
76. Wang X, Meng MQH. 2008. A fast algorithm for field computation in magnetic guidance. In *2008 International Conference on Information and Automation*, pp. 1608–13. Piscataway, NJ: IEEE
77. Schuerle S, Erni S, Flink M, Kratochvil BE, Nelson BJ. 2013. Three-dimensional magnetic manipulation of micro- and nanostructures for applications in life sciences. *IEEE Trans. Magn.* 49:321–30
78. Khalil ISM, Abelman L, Misra S. 2014. Magnetic-based motion control of paramagnetic microparticles with disturbance compensation. *IEEE Trans. Magn.* 50:1–10
79. Ongaro F, Heunis CM, Misra S. 2019. Precise model-free spline-based approach for magnetic field mapping. *IEEE Magn. Lett.* 10:2100405
80. Petruska AJ, Edelmann J, Nelson BJ. 2017. Model-based calibration for magnetic manipulation. *IEEE Trans. Magn.* 53:4900206
81. Mahoney AW, Abbott JJ. 2014. Generating rotating magnetic fields with a single permanent magnet for propulsion of untethered magnetic devices in a lumen. *IEEE Trans. Robot.* 30:411–20
82. Wright SE, Mahoney AW, Popek KM, Abbott JJ. 2017. The spherical-actuator-magnet manipulator: a permanent-magnet robotic end-effector. *IEEE Trans. Robot.* 33:1013–24
83. Hosney A, Klingner A, Misra S, Khalil IS. 2015. Propulsion and steering of helical magnetic microrobots using two synchronized rotating dipole fields in three-dimensional space. In *2015 IEEE/RSJ International Conference on Intelligent Robots and Systems*, pp. 1988–93. Piscataway, NJ: IEEE
84. Abbott JJ, Nagy Z, Beyeler F, Nelson BJ. 2007. Robotics in the small, part I: microrobotics. *IEEE Robot. Autom. Mag.* 14(2):92–103
85. Nelson BJ, Kaliakatsos IK, Abbott JJ. 2010. Microrobots for minimally invasive medicine. *Annu. Rev. Biomed. Eng.* 12:55–85
86. Diller E, Sitti M. 2013. Micro-scale mobile robotics. *Found. Trends Robot.* 2:143–259
87. Chen XZ, Hoop M, Mushtaq F, Siringil E, Hu C, et al. 2017. Recent developments in magnetically driven micro- and nanorobots. *Appl. Mater. Today* 9:37–48

88. Sitti M. 2017. *Mobile Microrobotics*. Cambridge, MA: MIT Press
89. Chowdhury S, Jing W, Cappelleri DJ. 2015. Controlling multiple microrobots: recent progress and future challenges. *J. Micro-Bio Robot.* 10:1–11
90. Diller E, Giltinan J, Sitti M. 2013. Independent control of multiple magnetic microrobots in three dimensions. *Int. J. Robot. Res.* 32:614–31
91. Khalil IS, Tabak AF, Hamed Y, Tawakol M, Klingner A, et al. 2018. Independent actuation of two-tailed microrobots. *IEEE Robot. Autom. Lett.* 3:1703–10
92. Salehizadeh M, Diller E. 2017. Two-agent formation control of magnetic microrobots in two dimensions. *J. Micro-Bio Robot.* 12:9–19
93. Cheang UK, Meshkati F, Kim H, Lee K, Fu HC, Kim MJ. 2016. Versatile microrobotics using simple modular subunits. *Sci. Rep.* 6:30472
94. Yu J, Yang L, Zhang L. 2018. Pattern generation and motion control of a vortex-like paramagnetic nanoparticle swarm. *Int. J. Robot. Res.* 37:912–30
95. Xie H, Sun M, Fan X, Lin Z, Chen W, et al. 2019. Reconfigurable magnetic microrobot swarm: multi-mode transformation, locomotion, and manipulation. *Sci. Robot.* 4:eav8006
96. Frei EH. 1970. Medical applications of magnetism. *Crit. Rev. Solid State Mater. Sci.* 1:381–407
97. Sliker LJ, Ciuti G, Rentschler M, Menciassi A. 2015. Magnetically driven medical devices: a review. *Expert Rev. Med. Devices* 12:737–52
98. Sliker LJ, Ciuti G. 2014. Flexible and capsule endoscopy for screening, diagnosis and treatment. *Expert Rev. Med. Devices* 11:649–66
99. Ciuti G, Calìo R, Camboni D, Neri L, Bianchi F, et al. 2016. Frontiers of robotic endoscopic capsules: a review. *J. Micro-Bio. Robot.* 11:1–18
100. Yim S, Sitti M. 2012. Design and rolling locomotion of a magnetically actuated soft capsule endoscope. *IEEE Trans. Robot.* 28:183–94
101. Chiba A, Sendoh M, Ishiyama K, Arai KI, Kawano H, et al. 2007. Magnetic actuator for a capsule endoscope navigation system. *J. Magnet.* 12:89–92
102. Popek KM, Hermans T, Abbott JJ. 2017. First demonstration of simultaneous localization and propulsion of a magnetic capsule in a lumen using a single rotating magnet. In *2017 IEEE International Conference on Robotics and Automation*, pp. 1154–60. Piscataway, NJ: IEEE
103. Slawinski PR, Taddese AZ, Musto KB, Obstein KL, Valdastrì P. 2017. Autonomous retroflexion of a magnetic flexible endoscope. *IEEE Robot. Autom. Lett.* 2:1352–59
104. Taddese AZ, Slawinski PR, Pirotta M, DeMomi E, Obstein KL, Valdastrì P. 2018. Enhanced real-time pose estimation for closed-loop robotic manipulation of magnetically actuated capsule endoscopes. *Int. J. Robot. Res.* 37:890–911
105. Tillander H. 1951. Magnetic guidance of a catheter with articulated steel tip. *Acta Radiol.* 35:62–64
106. Driller J, Frei EH. 1987. A review of medical applications of magnet attraction and detection. *J. Med. Eng. Technol.* 11:271–77
107. Lavie A. 1970. The swimming of the POD: theoretical analysis and experimental results. *IEEE Trans. Magn.* 6:365–67
108. Casarella WJ, Driller J, Hilal SK. 1969. The magnetically guided bronchial catheter of modified POD design: a new approach to selective bronchography. *Radiology* 93:930–32
109. Molcho J, Karny HZ, Frei EH, Askenasy HM. 1970. Selective cerebral catheterization. *IEEE Trans. Biomed. Eng.* BME-17:134–40
110. Penn RD, Hilal SK, Michelsen WJ, Goldensohn ES, Driller J. 1973. Intravascular intracranial EEG recording: technical note. *J. Neurosurg.* 38:239–43
111. Faddis MN, Lindsay BD. 2003. Magnetic catheter manipulation. *Coron. Artery Dis.* 14:25–27
112. Ernst S, Ouyang F, Linder C, Hertting K, Stahl F, et al. 2004. Initial experience with remote catheter ablation using a novel magnetic navigation system magnetic remote catheter ablation. *Circulation* 109:1472–75
113. Leon L, Warren FM, Abbott JJ. 2018. An in-vitro insertion-force study of magnetically guided lateral-wall cochlear-implant electrode arrays. *Otol. Neurotol.* 39:e63–73

114. Charreyron SL, Gabbi E, Boehler Q, Becker M, Nelson BJ. 2019. A magnetically steered endolaser probe for automated panretinal photocoagulation. *IEEE Robot. Autom. Lett.* 4:xvii–xxiii
115. Jeon S, Hoshlar AK, Kim K, Lee S, Kim E, et al. 2019. A magnetically controlled soft microrobot steering a guidewire in a three-dimensional phantom vascular network. *Soft Robot.* 6:54–68
116. Kim J, Kang B, Nguyen PB, Choi E, Kim CS, Park JO. 2018. Magnetic guidewire control without tip-angle detection in sharply curved blood vessel. In *2018 International Conference on Manipulation, Automation and Robotics at Small Scales*. Piscataway, NJ: IEEE. <https://doi.org/10.1109/MARSS.2018.8481187>
117. Chautems C, Nelson BJ. 2017. The tethered magnet: force and 5-DOF pose control for cardiac ablation. In *2017 IEEE International Conference on Robotics and Automation*, pp. 4837–42. Piscataway, NJ: IEEE
118. Boskma KJ, Scheggi S, Misra S. 2016. Closed-loop control of a magnetically-actuated catheter using two-dimensional ultrasound images. In *2016 6th IEEE International Conference on Biomedical Robotics and Biomechatronics*, pp. 61–66. Piscataway, NJ: IEEE
119. Le VN, Nguyen NH, Alameh K, Weerasooriya R, Pratten P. 2016. Accurate modeling and positioning of a magnetically controlled catheter tip. *Med. Phys.* 43:650–63
120. Liu T, Jackson R, Franson D, Lombard Poirot N, Criss RK, et al. 2017. Iterative Jacobian-based inverse kinematics and open-loop control of an MRI-guided magnetically actuated steerable catheter system. *IEEE/ASME Trans. Mechatron.* 22:1765–76
121. Ullrich F, Schuerle S, Pieters R, Dishy A, Michels S, Nelson BJ. 2014. Automated capsulorhexis based on a hybrid magnetic-mechanical actuation system. In *2014 IEEE International Conference on Robotics and Automation*, pp. 4387–92. Piscataway, NJ: IEEE
122. Greigarn T, Poirot NL, Xu X, Çavuşoğlu MC. 2018. Jacobian-based task-space motion planning for MRI-actuated continuum robots. *IEEE Robot. Autom. Lett.* 4:145–52
123. Tunay I. 2004. Position control of catheters using magnetic fields. In *Proceedings of the IEEE International Conference on Mechatronics, 2004*, pp. 392–97. Piscataway, NJ: IEEE
124. Tunay I. 2011. Distributed parameter statics of magnetic catheters. In *2011 Annual International Conference of the IEEE Engineering in Medicine and Biology Society*, pp. 8344–47. Piscataway, NJ: IEEE
125. Charreyron SL, Zeydan B, Nelson BJ. 2017. Shared control of a magnetic microcatheter for vitreoretinal targeted drug delivery. In *2017 IEEE International Conference on Robotics and Automation*, pp. 4843–48. Piscataway, NJ: IEEE
126. Kratchman LB, Bruns TL, Abbott JJ, Webster RJ III. 2017. Guiding elastic rods with a robot-manipulated magnet for medical applications. *IEEE Trans. Robot.* 33:227–33
127. Edelmann J, Petruska AJ, Nelson BJ. 2017. Magnetic control of continuum devices. *Int. J. Robot. Res.* 36:65–85
128. Peyron Q, Boehler Q, Rabenoroosa K, Nelson BJ, Renaud P, Andreff N. 2018. Kinematic analysis of magnetic continuum robots using continuation method and bifurcation analysis. *IEEE Robot. Autom. Lett.* 3:3646–53
129. Grady MS, Howard MA III, Dacey RG Jr., Blume W, Lawson M, et al. 2000. Experimental study of the magnetic stereotaxis system for catheter manipulation within the brain. *J. Neurosurg.* 93:282–88
130. Petruska AJ, Ruetz F, Hong A, Regli L, Surucu O, et al. 2016. Magnetic needle guidance for neurosurgery: initial design and proof of concept. In *2016 IEEE International Conference on Robotics and Automation*, pp. 4392–97. Piscataway, NJ: IEEE
131. Mathieu JB, Beaudoin G, Martel S. 2006. Method of propulsion of a ferromagnetic core in the cardiovascular system through magnetic gradients generated by an MRI system. *IEEE Trans. Biomed. Eng.* 53:292–99
132. Martel S. 2017. Beyond imaging: macro- and microscale medical robots actuated by clinical MRI scanners. *Sci. Robot.* 2:eam8119
133. Vartholomeos P, Fruchard M, Ferreira A, Mavroidis C. 2011. MRI-guided nanorobotic systems for therapeutic and diagnostic applications. *Annu. Rev. Biomed. Eng.* 13:157–84
134. Jeon SM, Jang GH, Choi HC, Park SH, Park JO. 2011. Precise manipulation of a microrobot in the pulsatile flow of human blood vessels using magnetic navigation system. *J. Appl. Phys.* 109:07B316
135. Vartholomeos P, Bergeles C, Qin L, Dupont PE. 2013. An MRI-powered and controlled actuator technology for tetherless robotic interventions. *Int. J. Robot. Res.* 32:1536–52

136. Felfoul O, Becker A, Bergeles C, Dupont PE. 2015. Achieving commutation control of an MRI-powered robot actuator. *IEEE Trans. Robot.* 31:387–99
137. Latulippe M, Martel S. 2018. Evaluation of the potential of dipole field navigation for the targeted delivery of therapeutic agents in a human vascular network. *IEEE Trans. Magn.* 54:5600112
138. Felfoul O, Becker AT, Fagogenis G, Dupont PE. 2016. Simultaneous steering and imaging of magnetic particles using MRI toward delivery of therapeutics. *Sci. Rep.* 6:33567
139. de Jong S. 2010. Presenting the cyclotactor project. In *TEI '10: Proceedings of the Fourth International Conference on Tangible, Embedded, and Embodied Interaction*, pp. 319–20. New York: ACM
140. Pedram SA, Klatzky RL, Berkelman P. 2017. Torque contribution to haptic rendering of virtual textures. *IEEE Trans. Haptics* 10:567–79
141. Zhang R, Boyles AJ, Abbott JJ. 2018. Six principal modes of vibrotactile display via stylus. In *2018 IEEE Haptics Symposium*, pp. 313–18. Piscataway, NJ: IEEE
142. Jenkins AW, Parker HM. 1959. Electromagnetic support arrangement with three-dimensional control. I. Theoretical. *J. Appl. Phys.* 30:S238–39
143. Fosque HS, Miller G. 1959. Electromagnetic support arrangement with three-dimensional control. II. Experimental. *J. Appl. Phys.* 30:S240–41
144. Abbott JJ, Brink JB, Osting B. 2017. Computing minimum-power dipole solutions for interdipole forces using nonlinear constrained optimization with application to electromagnetic formation flight. *IEEE Robot. Autom. Lett.* 2:1008–14



Contents

Robotic Self-Replication <i>Matthew S. Moses and Gregory S. Chirikjian</i>	1
Robots That Use Language <i>Stefanie Tellex, Nakul Gopalan, Hadas Kress-Gazit, and Cynthia Matuszek</i>	25
Magnetic Methods in Robotics <i>Jake J. Abbott, Eric Diller, and Andrew J. Petruska</i>	57
Mobile Sensor Networks and Control: Adaptive Sampling of Spatiotemporal Processes <i>Derek A. Paley and Artur Wolek</i>	91
Network Effects on the Robustness of Dynamic Systems <i>Ketan Savla, Jeff S. Shamma, and Munther A. Dableh</i>	115
Routing on Traffic Networks Incorporating Past Memory up to Real-Time Information on the Network State <i>Alexander Keimer and Alexandre Bayen</i>	151
Amphibious and Sprawling Locomotion: From Biology to Robotics and Back <i>Auke J. Ijspeert</i>	173
Stochastic Dynamical Modeling of Turbulent Flows <i>A. Zare, T.T. Georgiou, and M.R. Jovanović</i>	195
Robotics In Vivo: A Perspective on Human–Robot Interaction in Surgical Robotics <i>Alaa Eldin Abdelaal, Prateek Mathur, and Septimiu E. Salcudean</i>	221
The Synergy Between Neuroscience and Control Theory: The Nervous System as Inspiration for Hard Control Challenges <i>Manu S. Madhav and Noah J. Cowan</i>	243
Learning-Based Model Predictive Control: Toward Safe Learning in Control <i>Lukas Hewing, Kim P. Wabersich, Marcel Menner, and Melanie N. Zeilinger</i>	269

Recent Advances in Robot Learning from Demonstration <i>Harish Ravichandar, Athanasios S. Polydoros, Sonia Chernova, and Aude Billard</i>	297
Recent Scalability Improvements for Semidefinite Programming with Applications in Machine Learning, Control, and Robotics <i>Anirudha Majumdar, Georgina Hall, and Amir Ali Ahmadi</i>	331
The Inerter: A Retrospective <i>Malcolm C. Smith</i>	361
Port-Hamiltonian Modeling for Control <i>Arjan van der Schaft</i>	393
Automated Planning for Robotics <i>Erez Karpas and Daniele Magazzeni</i>	417
Scientific and Technological Challenges in RoboCup <i>Minoru Asada and Oskar von Stryk</i>	441

Errata

An online log of corrections to *Annual Review of Control, Robotics, and Autonomous Systems* articles may be found at <http://www.annualreviews.org/errata/control>